Supplementary Information

Engineering MOF/Carbon Nitride Heterojunctions for Effective Dual CO₂ Conversion and OER Photocatalysis

Valentin Diez-Cabanes[a†], Kevin Granados-Tavera[a,b†], Inderdip Shere[a†], Gloria Cárdenas-Jirón[b], Guillaume Maurin[a,*]

[1] ICGM, Univ. Montpellier, CNRS, ENSCM, Montpellier, 34293, France

[2] Laboratory of Theoretical Chemistry, Faculty of Chemistry and Biology, University of Santiago de Chile (USACH), 9170022, Santiago, Chile.

Table of Contents

S1. Computational details

S1.1. Construction of the MOF/PHI-M heterojunctions

S1.1.1 Geometry optimization of the MIP-177 crystal

The pristine MIP-177 was first geometry optimized at the density functional theory (DFT) level using the Vienna ab initio simulation (VASP) package version 5.4.[1] The electron-ion interaction was described using the projector augmented wave (PAW) method.[2] The plane waves with an energy cutoff of 520 eV were used to expand the generalized gradient approximation (GGA), Perdew-Burke-Ernzerhof (PBE) functional,[3] and electron wave function. The Gaussian smearing with a width of 0.05 eV was used for integrating the Brillouin zone. The long-range van der Waals dispersion forces were estimated by the DFT-D3 method of Grimme with zero damping function.[4] The Monkhorst-Pack Γ-centred mesh of 3×3×3 was used to sample the Brillouin zone of the MOF structure. The relaxation of the electronic degree of freedom was achieved by setting the total energy to 10^{-4} eV and force between atoms of 0.01 eV/Å in the self-consistency loop.

Table S1. Cell parameters for the DFT and FF-MD optimized MIP-177 structure vs experimental data alongside the cell parameters for the DFT- and FF-MD optimized MIP-177 slab model.

Cell parameters	a (Å)	b (Å)	c (Å)	α (°)	β (°)	γ (°)
Bulk structure						
Exp[5]	22.594	22.594	12.307	90	90	120
DFT	22.595	22.595	12.307	90	90	120
FF-MD	23.531	23.531	12.861	90	90	120
Slab Model						
DFT	22.595	22.595	61.534	90	90	120
FF-MD	23.531	23.531	61.534	90	90	120

S1.1.2 Force-field parameters for the MIP-177 [001]and [110] surface slab models

Note that the intermolecular Lennard-Jones (LJ) parameters were taken from the UFF potential without any refinement. They are reported in Table S2 for each atom type present in MOF. The intra-molecular force-field parameters for the MOF surface slab model were adjusted from those available in the universal force-field (UFF) potential[6]. The corresponding adjusted bonding and bending parameters are provided in Tables S3 and S4 with the atom types described in Figure S3. Regarding the dihedral and improper angle potential parameters, they

were kept as they are defined in UFF (Table S5). The potential parameter adjustment was achieved with the objective to obtain a good agreement between the DFT and the force field-MD optimized structural features for both the MOF bulk and the MOF slab model. The comparison between force field MD and DFT-derived cell parameters is reported in Table S1 while the mean-value of bond distances, bending angles, and dihedral angles of the MD-equilibrated crystal structure and the corresponding geometric features obtained for the DFT optimized structure are reported in Table S7. These force field MD simulations were run for 1 ns using Gromacs-5.1.4 software[7] and considering a simulation box of $47.1 \times 47.1 \times 38.5 \text{Å}$ for the MIP-177 crystal structure.

Cleaved plane [001]

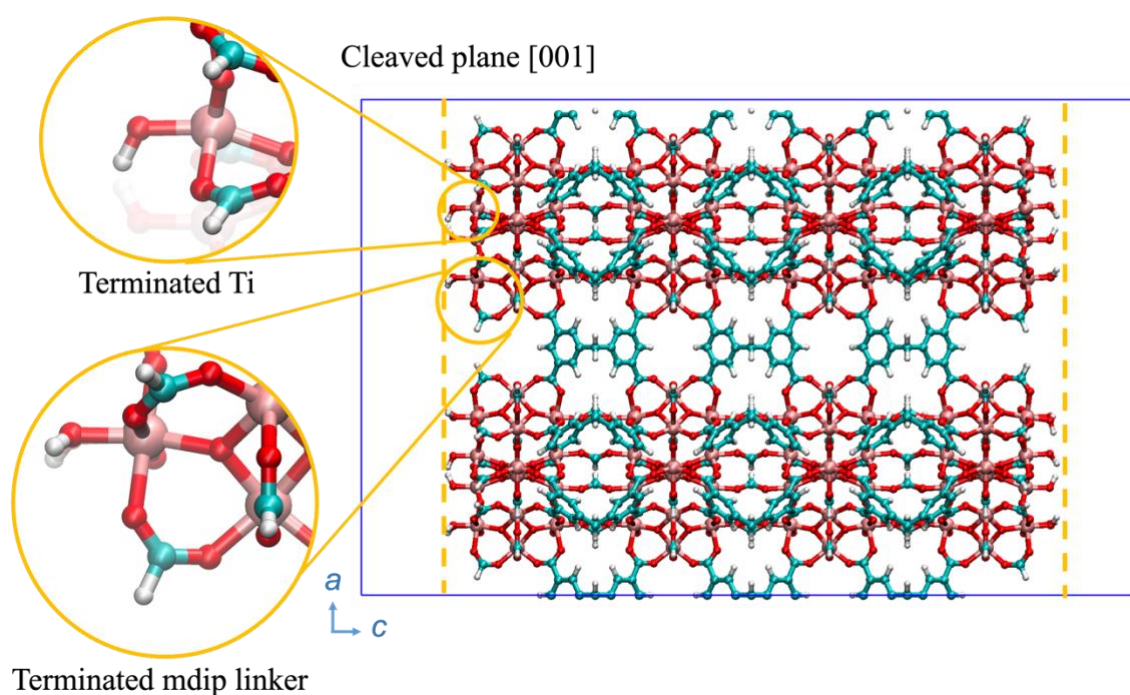Terminated Ti

Terminated mdip linker

Figure S1. Construction of the MOF [001] slab model cleaved from the bulk MOF. Regarding the termination, the OH -group dissociated from the water molecule forms Ti-OH termination, and the remaining hydrogen atom serves as termination for the organic linker side.
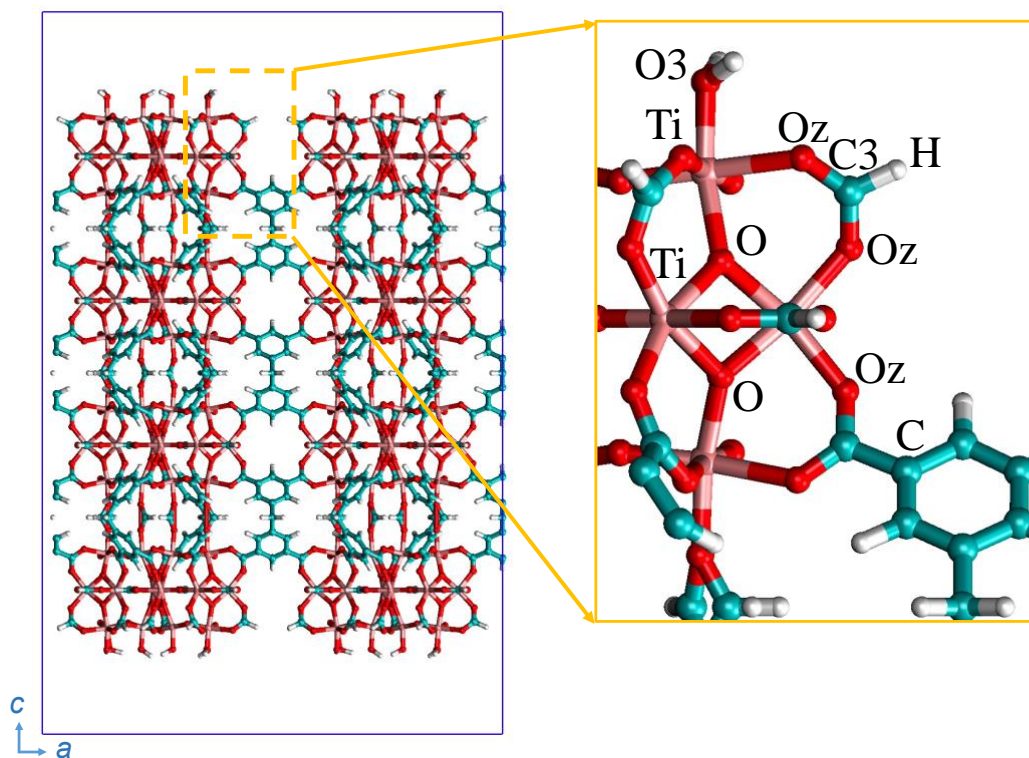
Figure S2. Illustration of the geometry optimized MOF [001] slab model with the different atom types used to define the FF-based model in this work.

The DFT-optimized MOF structure was reshaped and was repeated to obtain a dimension of 39.14 × 77.16 × 36.92 Å. The crystallographic [110] plane was cleaved from the MOF bulk only via the mdip linker (Figure S3). The cleaved linker is saturated with hydrogen atoms to maintain the charge neutrality of the structure. Around 20 Å of vacuum space was included in the MOF [110] slab model to prevent surface self-interaction. Types of atoms identified in the model are depicted in Figure S3, and the corresponding force field parameters are tabulated in Table S2.
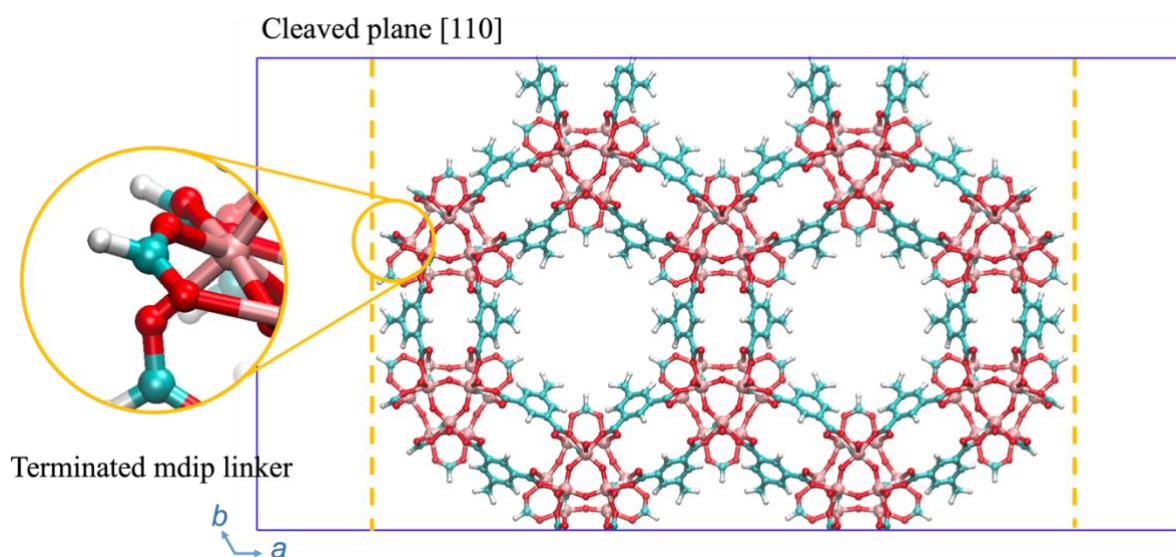
Figure S3. Construction of the MOF [110] slab model by cutting the mdip-linker and saturating the terminal organic linker by hydrogen atoms.
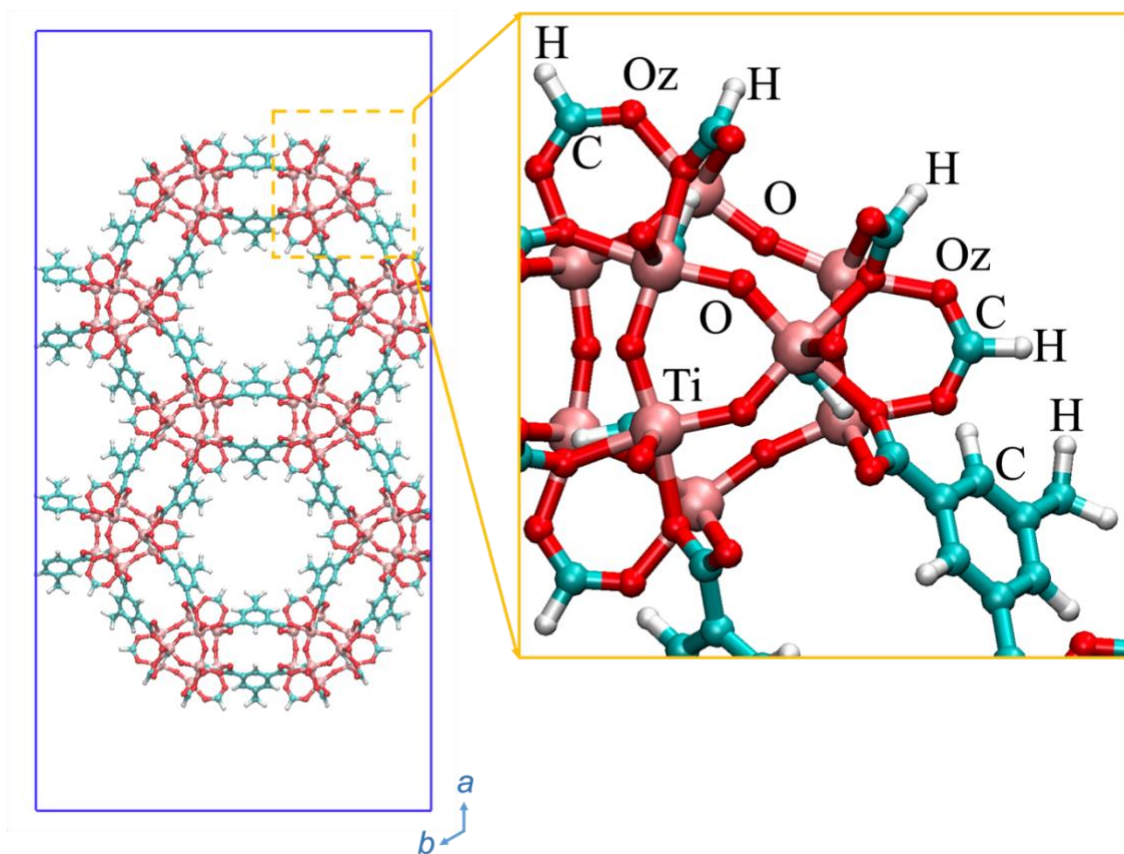
Figure S4. Illustration of the geometry optimized MOF [110] slab model with the different atom types used to define the FF-based model in this work.

Table S2. LJ parameters for the atom types defined in Figures S2 and S4.

Atom type	σ (Å)	ε(kJ/mol)
Ti	2.829	0.071159
H	2.571	0.184208
O	3.118	0.251147
Oz	3.118	0.251147
O3	3.118	0.251147
C	3.431	0.440342
C3	3.431	0.440342

Table S3. Bond potential parameters for the atom pairs in MOF ($U_B = \frac{K_B}{2}(r - r_0)^2$, where K_B is the harmonic bond potential and r_0 is equilibrium bond distance).

Sno.	Bond	r_0 (Å)	K_B (kJ mol^{-1} Å $^{-2}$)
1	Ti-O	1.977	1995.93
2	Ti-Oz	1.977	1995.93
3	H-C	1.097	2881.96
4	H-C3	1.097	2881.96
5	O-C	1.275	5981.99
6	C-C	1.395	3873.16
7	C-C	1.485	3278.90
8	C3-C	1.515	3097.02

Table S4. Angle potential parameters for the atom sequences in the MOF ($U_A = \frac{K_A}{2}(\cos \theta - \cos \theta_0)^2$, where K_A is the harmonic angle potential force constant and θ_0 is equilibrium angle).

Sno.	Angle	θ_0	K_A (kJ mol^{-1})
1	O-Ti-Oz	90	1421.2
2	O-Ti-O	90	1421.2
3	Oz-Ti-Oz	78.5	1600.8
4	Ti-Oz-C	133	1067.0
5	Ti-Oz-Ti	120	970.5
6	Ti-O-Ti	148	829.3
7	H-C-C	120	777.5
8	C-C-C	120	1510.5
9	C-C-C	120	1386.8
10	O-C-O	124	2806.3
11	O-C-C	117	1869.0
12	H-C-O	117	1084.8
13	H-C3-H	107	355.5
14	H-C3-C	109	573.4
15	C-C3-C	108	1066.8
16	C-C-C3	120	1345.4

Table S5. Dihedral angle parameters for the atom sequences identified in the MOF. ($U_D = K_D(1 + (\cos(2\emptyset - \emptyset_0))^2$, where K_D is the periodic dihedral angle potential force constant with $\emptyset_0$ is equilibrium angle).

Sno.	Dihedral angle	$\emptyset_0$ (deg)	K_D (kJ mol^{-1})
1	Oz-C-C-C	180	2.325
2	C-C-Oz-Ti	180	9.4
3	C-C-C-C	180	6.267
4	C-C-C3-C	0	0.349
5	C-C3-C-C	180	1.744

Regarding the MOF surface slab model, we added the potential parameters to describe the bond, and bending terms involving the -OH terminal functions using UFF. Additionally, torsional potentials were applied to restrict the movement of the terminal groups. The equilibrium parameters were again adjusted to the DFT-optimized geometry. These additional parameters are summarized in Table S6. Here force field MD NVT ensemble simulations were run for 10 ns with a time step of 2 fs using Berendsen thermostat with a time constant of 0.1 ps. Simulations were performed using Gromacs-5.1.4 software,[7] and considering a simulation box of $47.1 \times 47.1 \times 61.5$ Å of the MOF surface slab model.

Table S6. Additional force field parameters related to the terminal -OH functions of the MOF surface slab model.

Bond		r_0 (Å)	K_B (kJ mol^{-1} Å^{-2})
1	Ti-O3	1.875	1776.5
2	H-O3	0.975	4688.1
Angles		θ_0	K_A (kJ mol^{-1})
1	Ti-O3-H	116.74	378.4
2	Oz-Ti-O3	93.32	1344.8
3	O-Ti-O3	160.00	1446.8
Dihedral		θ_0	K_A (kJ mol^{-1})
1	Oz-Ti-O3-H	0	9.4

The DFT-derived partial charges of the MOF surface slab model are incorporated in the cif file provided as (https://github.com/InderdipShere/MIP177_PHIM_composite) Supplementary information.

Table S7. Comparison between DFT-derived bond, angle, dihedral force field parameters for the MOF bulk as well as the Force field derived values for the MOF in the MOF/PHI-M heterojunctions.

Bond(Å)		DFT Bulk	FF-MD Bulk	FF-MD MOF/PHI-H	FF-MD MOF/PHI-K^+	FF-MD MOF/PHI-Co^{2+}
1	Ti-O	1.977	2.115	2.147	1.845	1.845
2	Ti-Oz	1.977	2.115	2.175	1.739	1.725
3	H-C	1.097	1.095	1.095	1.095	1.095
4	H-C3	1.097	1.095	1.095	1.095	1.095
5	O-C	1.275	1.305	1.305	1.245	1.245
6	C-C	1.395	1.395	1.395	1.635	1.635
7	C-C	1.485	1.485	1.455	1.425	1.425
8	C3-C	1.515	1.515	1.515	1.545	1.515
Angles (°)						
1	O-Ti-Oz	90	90.0	90.8	90.4	91.0
2	O-Ti-O	90	90.0	92.3	89.9	89.5
3	Oz-Ti-Oz	78.5	75.2	77.1	74.8	74.6
4	Ti-Oz-C	133	131.9	133.2	127.7	127.4
5	Ti-Oz-Ti	120	128.7	130.7	127.3	127.0
6	Ti-O-Ti	148	153.3	157.6	142.7	143.1
7	H-C-C	120	119.0	119.3	118.7	118.6
8	C-C-C	120	118.7	119.6	122.0	122.0
9	C-C-C	120	118.7	119.3	127.4	127.7
10	O-C-O	124	126.0	126.7	119.3	119.2
11	O-C-C	117	115.8	115.3	119.7	120.0
12	H-C-O	117	116.8	117.4	118.0	118.3
13	H-C3-H	107	107.7	104.6	106.3	106.1
14	H-C3-C	109	109.8	110.0	110.0	110.2
15	C-C3-C	108	108.1	110.5	106.9	107.0
16	C-C-C3	120	119.2	119.6	118.3	118.4
Dihedral (°)						
1	Oz-C-C-C	180	180	176.7	176.4	176.4
2	C-C-Oz-Ti	180	180	176.5	177.0	177.4
3	C-C-C-C	180	180	176.1	175.9	176.1
4	C-C-C3-C	0	0	5.6	7.8	7.2
5	C-C3-C-C	180	180	172.2	175.4	175.7

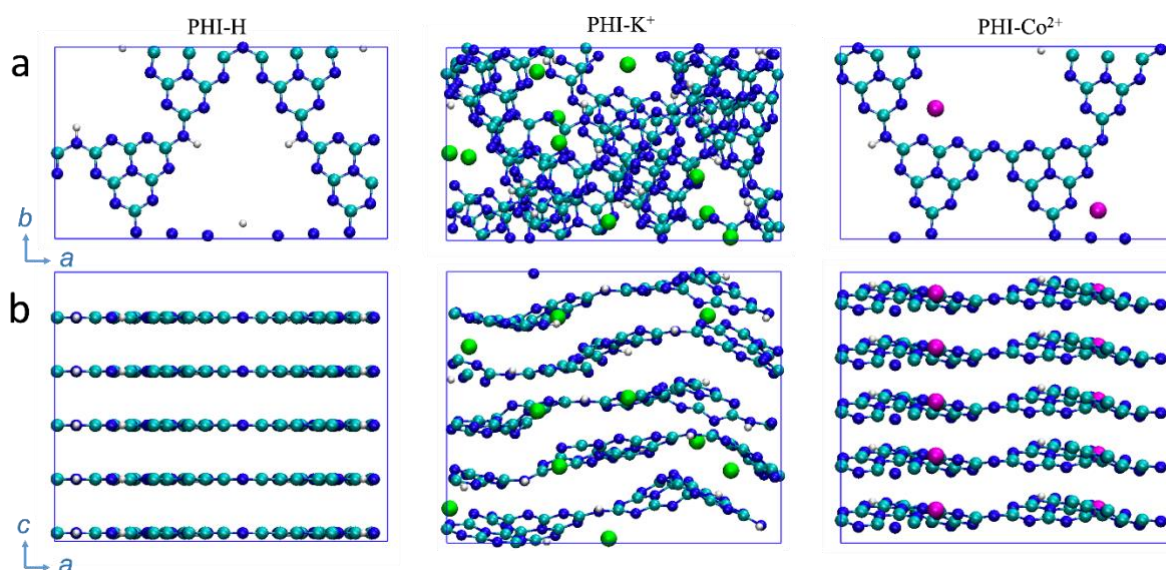*S1.1.3 DFT-optimized PHI-M structure models*

Figure S5. DFT-optimized structures of the five layers models of PHI-H, PHI-K$^+$, and PHI-Co^{2+} along **a)** [001] and **b)** [100] directions. Carbon, nitrogen and hydrogen atoms are represented by cyan, blue and white spheres, whereas cations K$^+$ and Co^{2+} are represented by green and magenta spheres, respectively.

In order to obtain a quantitative estimation of the distortion of our DFT-geometry optimized five-layers PHI-M periodic models we computed the averaged deviation with respect to the planar geometry (Δz) by employing the following formula:

$$\overline{\Delta z} = \frac{\sum_n |z_m - z_i|}{n} \tag{Eq. S1}$$

Being z_m and z_i the coordinates in the normal plane direction of the mass centre and the individual atoms of the PHI-M DFT-structures. The resulting calculated Δz values for the 5 layers of each PHI-M and the corresponding averaged values are reported in Table S8.

Table S8. Mean deviation of the normal coordinates with respect to their mass centre for the PHI-M layer models obtained for the DFT-optimized PHI-M periodic structure, the force-field based MD PHI-M optimized structure, and the DFT-optimized PHI-M structure in the heterojunction cluster model.

Δz (Å)	DFT-bulk			FF-MD bulk			DFT-heterojunction cluster		
	PHI-H	PHI-K$^+$	PHI-Co^{2+}	PHI-H	PHI-K$^+$	PHI-Co^{2+}	PHI-H	PHI-K$^+$	PHI-Co^{2+}
1	0.001	1.053	0.474	0.314	0.824	0.765	-	-	-
2	0.001	0.843	0.367	0.321	0.784	0.765	-	-	-
3	0.001	0.816	0.376	0.307	0.841	0.769	-	-	-
4	0.001	0.897	0.393	0.312	0.858	0.728	-	-	-
5	0.001	1.023	0.387	0.333	0.926	0.723	-	-	-
μ	0.001	0.926	0.400	0.317	0.846	0.750	0.295	0.239	0.816

S1.1.4 Force field parameters for PHI-M structure models

The optimized potential for the liquid simulation-all atom (OPLS-AA)[8] parameters were used for representing the intra-molecular terms (bond, angle, dihedral, and improper potential) and adjusted accordingly to get a good agreement between the force-field MD derived parameters and those obtained for the DFT-optimized structure. For both K$^+$ and Co^{2+} cations, UFF intermolecular parameters were used. For these systems, force field MD NVT ensemble simulations were run for 10 ns with time step of 1 fs using Berendsen thermostat with time constant of 0.1 ps. Simulations were performed employing Gromacs-5.1.4 software,[7] and considering a simulation box of $47.1 \times 40.8 \times 35$ Å for all PHI-Ms.
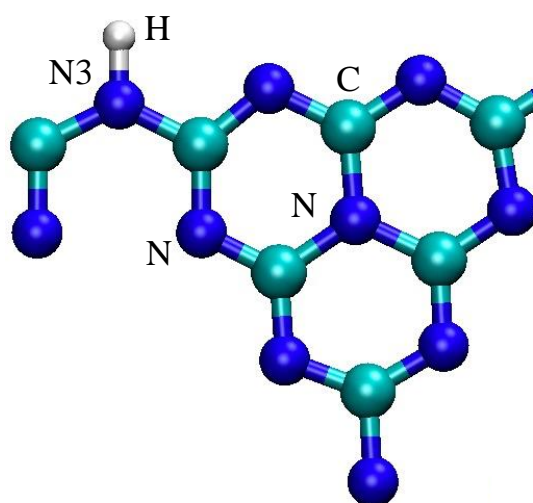

Figure S6. Illustration of the PHI-H model with the different atom types.

.

Table S9. Force field parameters for PHI-M.

Bond		r_0 (Å)	K_B (kJ mol^{-1} Å^{-2})
1	C-N	1.34	4100.32
2	C-N3	1.38	4100.32
3	N3-H	1.04	3631.71
Angles		θ_0	K_A (kJ mol^{-1})
1	C-N-C	116	585.76
2	C-N3-C	128	585.76
3	N-C-N	120	585.76
4	N-C-N3	116	585.76
5	C-N3-H	115	292.88
Dihedral		θ_0	K_A (kJ mol^{-1})
1	N-C-N-C	180	9.4
2	N-C-N3-C	180	6.2
Improper		θ_0	K_A (kJ mol^{-1})
1	N-C-N-N	0	6.8

The DFT-derived partial charges of the PHI-M slab model are incorporated in the cif file provided as Supplementary (https://github.com/InderdipShere/MIP177_PHIM_composite) information.

Table S10. Comparison between DFT-derived bond, bending angles and dihedral angles for the PHI-H bulk, and for the PHI-M in the MOF/PHI-M heterojunction models.

Bond (Å)		DFT Bulk	FF-MD Bulk	FF-MD MOF/PHI-H	FF-MD MOF/PHI-K⁺	FF-MD MOF/PHI-Co²⁺
1	C-N	1.34	1.35	1.39	1.39	1.49
2	C-N3	1.38	1.35	1.39	1.39	1.49
3	N3-H	1.04	1.05	1.04	1.04	1.13
Angles (°)						
1	C-N-C	116	118.7	119.5	119.0	119.7
2	C-N3-C	128	117.4	133.9	129.1	126.7
3	N-C-N	120	118.7	119.7	119.8	119.5
4	N-C-N3	116	134.4	118.4	119.3	119.3
5	C-N3-H	115	111.1	111.4	111.7	112.9
Dihedral (°)						
1	N-C-N-C	180	180	179.8	176.4	176.6
2	N-C-N3-C	180	180	179.9	178.7	176.4
Improper (°)						
1	N-C-N-N	0	0	1.3	4.3	3.6

S1.1.5 Equilibration procedure of MOF/PHI-M heterojunction

The following procedure was used to equilibrate all systems:

a. Energy minimization: To eliminate the close overlaps between atoms.

   A maximum of 10000 energy minimization steps is performed to achieve the maximum force of 1000 kJ mol⁻¹nm⁻¹ using the steepest descent algorithm with a step size of 0.01.

b. NPT simulation: To allow MIP-177 and PHI layers to interact and obtain the equilibrium configuration.

   NPT simulation was performed for 1 ns with a time step of 1 fs. A modified Berendsen thermostat was used for temperature coupling with a time constant of 100 fs. An anisotropic pressure coupling (Area in *x-y* direction and *z* dimension) was performed using the Parrinello-Rahman thermostat with a time constant of 10 ps.

c. NVT simulation: To allow system to achieve equilibrium configuration without being influenced by the initial configuration.

   NVT simulation was carried out for 1 ns with the time step of 1 fs using the modified Berendsen thermostat with the time constant of 100 fs.

The equilibrium procedure was performed at 298 K and 1 bar. The short-range interaction was considered with the cut-off distance of 14 Å, and long-range interactions were handled using

the Ewald summation technique. We calculated the total energy of the system (Figure S7) to verify that the system has achieved the equilibrium configuration. A small fluctuation in the mean system energy verifies that the system is well equilibrated.
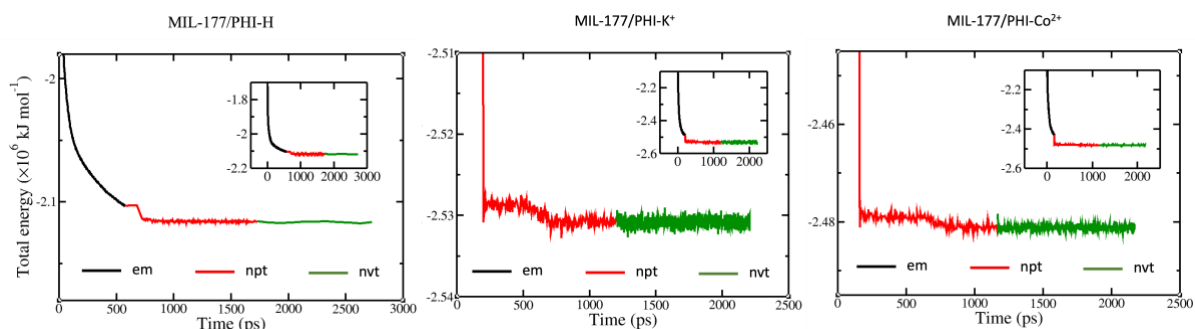

Figure S7. The evolution of the total energy of the system during energy minimization, NPT simulation, and NVT simulation were conducted during the equilibration process. The inset shows a zoom-out version of the total energy from the initial configuration. Smaller fluctuation of total energy around the mean value during NVT simulation verifies that the system has achieved equilibrium configuration.

All the Gromacs parameters files (em.mdp, npt.mdp and nvt.mdp) are available in the GitHub repository (https://github.com/InderdipShere/MIP177_PHIM_composite). After the equilibration procedure, the equilibrated system is analyzed for its properties in the production moves.

S1.2. MOF/PHI-M heterojunction cluster models

S1.2.1 Geometry optimization
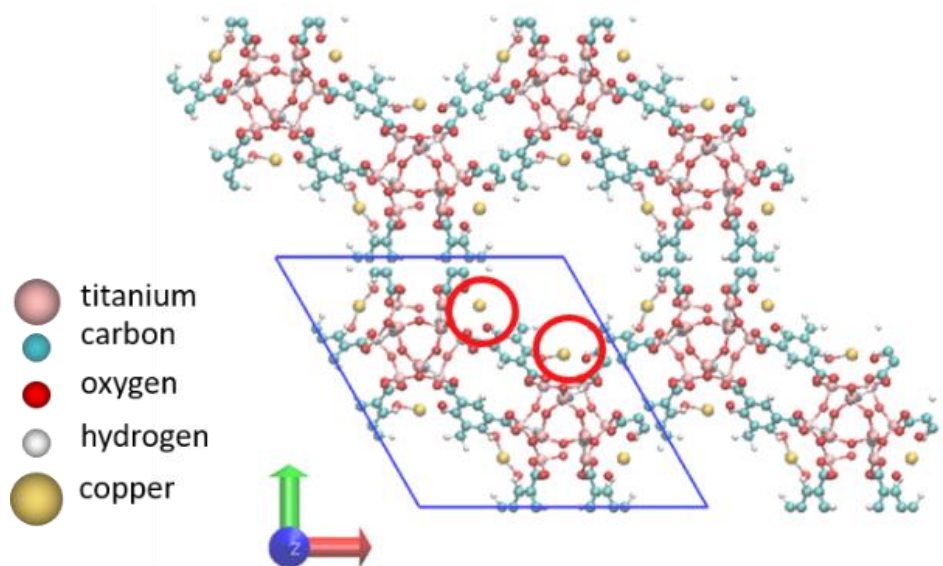
Figure S8. Top view of the relaxed unit cell of the Cu$^+$@MOF bulk structure.

The geometries of the MOF/PHI-M heterojunction clusters were optimized by means of DFT calculations using the PBE functional[9] for both exchange and correlation parts, and Grimme's DFT-D3 method for the empirical dispersion.[10] The calculations for MOF/PHI-Co^{2+} and Cu$^+$@MOF/PHI-Co^{2+} were performed with spin polarization. We used the Hubbard on-site potential (U)[11] to d orbitals of cobalt, with U=3.7 eV in line with previous works performed on Co^{2+}-based systems.[12] We used a double-ζ-polarized (DZP) basis set, along with PseudoDojo norm-conserving pseudopotentials[13] to represent all atoms. All geometry optimizations of the heterojunction cluster models were carried out within the Quantum ATK package.[14]

S2.2.2 Electronic properties

The ground state (GS) properties of the optimized heterojunction cluster models were computed within the hybrid Heyd–Scuseria–Ernzerhof (HSE06) functional[15] within a 6-31G(d,p) basis set[16] for the C, H, O, N, K, Co and Cu atomic species, and LanL2DZ basis[17] for the Ti atoms. All these calculations were performed within the Gaussian 09 program package.[18] Notably, we verified that our models (isolated MOF or PHI-M clusters within the same geometry as the heterojunction cluster models) are able to mimic the electronic structure of the bulk materials. In the case of the isolated PHI-M cluster models, Table S11 shows the comparison between the calculated band edge energies and the experimental values measured by photoemission spectroscopy, both estimates showing a remarkable agreement. For the isolated MOF clusters, we inserted these models in a 30x30x30Å unit cell and compared the computed bandgap with the one obtained for the bulk experimental cell. These periodic calculations were performed at the Γ point within the HSE06 functional[15] expanded in a plane-wave basis set with an energy cutoff of 300 eV, as implemented by adopting the PAW pseudopotentials[19] in the VASP code. The identical bandgaps obtained for the cluster (2.44 eV) vs bulk (2.53 eV) systems clearly corroborates the suitability of our models to study the MOF interfaces and evidenced that the electronic properties of MOF are mainly driven by one single Ti$_{12}$O$_{15}$ oxocluster. On the same vein, we compared the excited state properties of the lowest energy region of the cluster vs periodic Cu$^+$@MOF models. These calculations were conducted by relying on the Time-Dependent Density Functional Perturbation Theory (TD-DFPT) linear response approach,[20] as it is implemented in the CP2K package,[21] and on the same computational set up as the one employed in a former work.[22] Interestingly, both cluster and periodic models displayed similar absorption edges (see Figure S9) and, more importantly, the most relevant states belonging to

these region exhibited a marked metal-to-core CT character, regardless the model considered, as it is showed by their corresponding Natural Transition Orbitals (NTOs)[23] depicted in Figure S10. Finally, further details about the benchmarking of the opto-electronic properties of our cation loaded MOF and PHI cluster models against the available absorption/photoemission spectroscopic measurements and the computed bulk properties, can be found in refs. S24 and S25, respectively.

Table S11. VB maximum (VBM) and CB minimum (CBM) energies in eV with respect to the vacuum level, as estimated by DFT (*theo*) and by photoemission (*exp*) measurements.[26,27]

	Theo		*exp*	
system	VBM	CBM	VBM	CBM
PHI-H	-6.8	-4.0	-6.0	-3.5
PHI-K$^+$	-6.4	-3.7	-6.7	-4.0
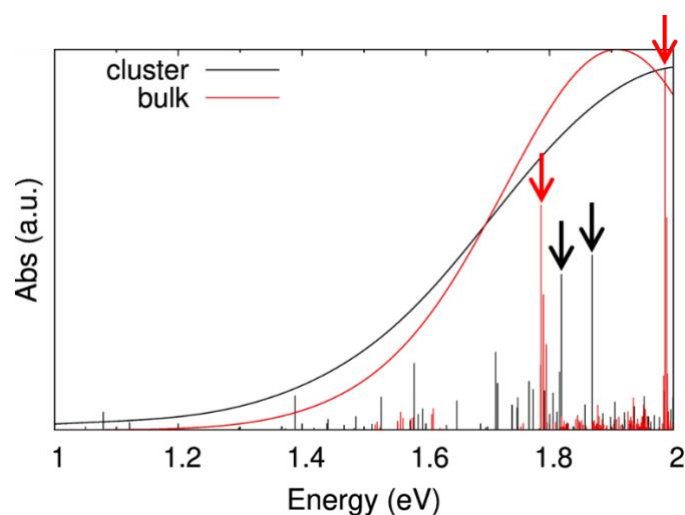
Figure S9. TD-DFPT simulated absorption spectra of the lowest energy region for cluster (black) and periodic (red) Cu$^+$@MOF models.
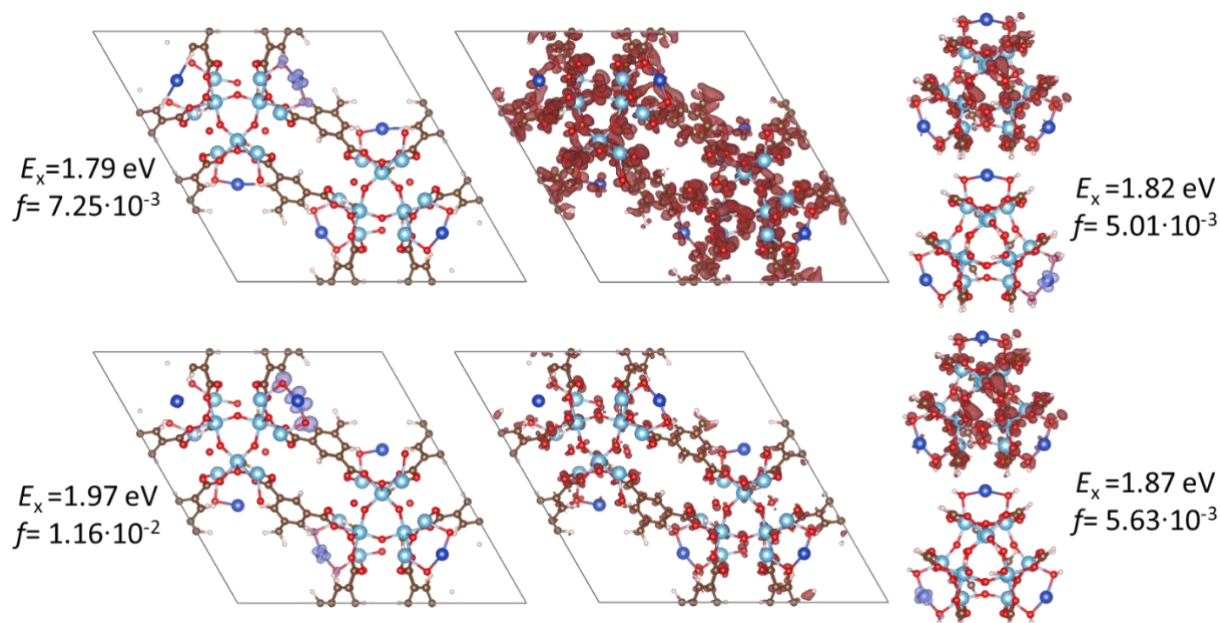
Figure S10. NTO shapes for the occupied/virtual (purple/red) orbitals of the most relevant states pointed with arrows in Figure S9. The isodensity value used to represent the isodensity plots was set to 0.1 a.u.

S1.2.3 TD-DFT and sTD-DFT calculations

Within the sTD-DFT approach the most computational demanding steps of the TD-DFT frame corresponding to the computation of the two-electron integrals matrix elements of Casida's equations, are evaluated by coulombic interactions described by means of Mataga-Nishimoto-Ohno-Klopman damped operators. These operators are built by fitting two global parameters α and β which, in the case of standard hybrid functionals, are determined as a function of their amount of non-local Fock exchange a_x but, unfortunately, the fitting parameters for the HSE06 functional (a_x=0.25) are still not available in the literature. In this context, we employed the reference isolated PHI-K^+ cluster as test model to fit the parameters α and β of the sTDA technique, and to benchmark the suitability of employing the Tamm-Dancoff Approximation (TDA)[28] to reduce the computational cost of the TD-DFT calculations. As it is illustrated in Figure S11, the identical VIS absorption features observed when employing the simplified TDA scheme (sTDA) with α=1 and β=0.25 fitting values, with respect to the spectra computed with the TDA and the full TD-DFT approaches, validates the choice of our methodology.
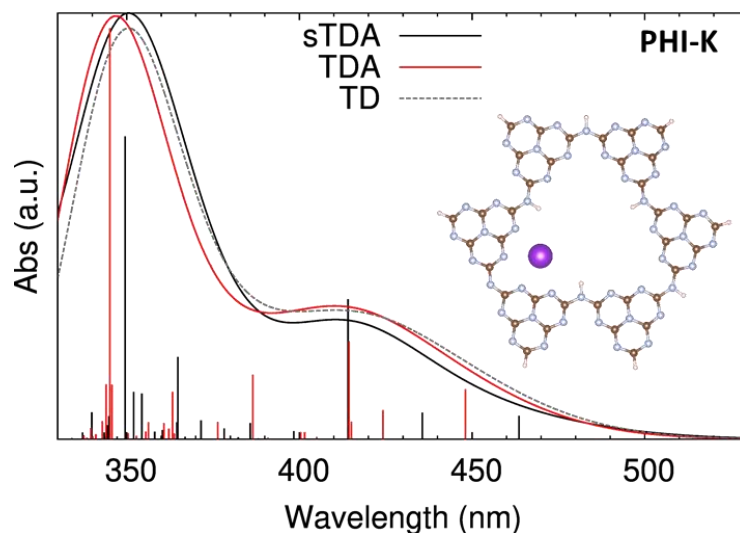
Figure S7. Simulated absorption spectra of the PHI-K$^+$ layer computed at the sTDA (black), TDA (red) and full TD-DFT (dashed grey line) levels of theory. Vertical lines correspond to the main transitions composing the spectra.

As a further step, we tested the capacity of our sTDA approach to fairly reproduce the main absorption characteristics of the MOF/PHI-K$^+$ composites, by comparing the properties of the main vertical transitions conforming the simulated spectrum with those computed at the full TDA level (see Figure S12 and Table S13).
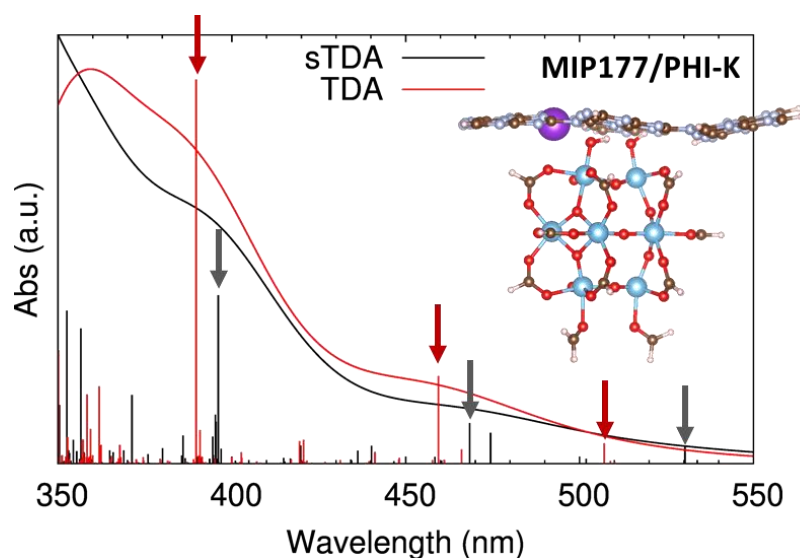
Figure S8. Simulated absorption spectra of the MOF/PHI-K$^+$ heterojunction cluster model computed at the sTDA (black) and TDA (red) levels of theory. Vertical lines correspond to the transitions composing the spectra. Vertical arrows were employed to depict the most important states dictating the absorption features of the spectra.

Table S12. Main excited state properties for the vertical transitions highlighted with red and black arrows in Figure S12 for the spectra computed at the sTDA and TDA levels, respectively: number of state (n), exciton energies (E) and wavelengths (λ), oscillator strengths (f) and main occupied-virtual orbital transition composing each state with their corresponding weight in parenthesis.

		sTDA					TDA		
n	E(eV)	λ(nm)	f(a.u.)	Transition	n	E(eV)	λ(nm)	f(a.u.)	Transition
60	2.34	530	0.010	H→L+18 (1.00)	70	2.45	507	0.012	H→L+18 (0.70)
125	2.65	468	0.024	H→L+25 (0.88)	127	2.70	459	0.051	H→L+25 (0.62)
293	3.13	396	0.098	H→L+33 (0.62) H-2→L+24 (0.52)	297	3.18	390	0.223	H→L+36 (0.43) H-4→L+25 (0.33)

Despite the different absorption energies of the main excited states composing their spectrum, the overall shape of the spectra computed at the sTDA and TDA levels is equivalent. More importantly, the nature of the orbital transitions constituting these states is identical for both approaches. Finally, all computed vertical transitions were convoluted with a Gaussian function with a half-width at full-length of σ=0.15 eV to estimate all simulated spectra. Note at this point in order to evaluate the absorption properties of the MOF/PHI-K$^+$ heterojunction cluster model in the full VIS region we had to reduce the level of accuracy of the basis set (from 6-31G(d,p) to 3-21G*). It is important to stress that this represents a common strategy to compute the excited states of large TiO$_2$-based clusters,[29] and in our particular case it was not translated to a substantial loss of accuracy, as it can be observed by comparing the sTDA simulated spectra for all composites calculated with the 3-21G* basis set with respect to the ones obtained with 6-31G(d,p) (see Figure S13).
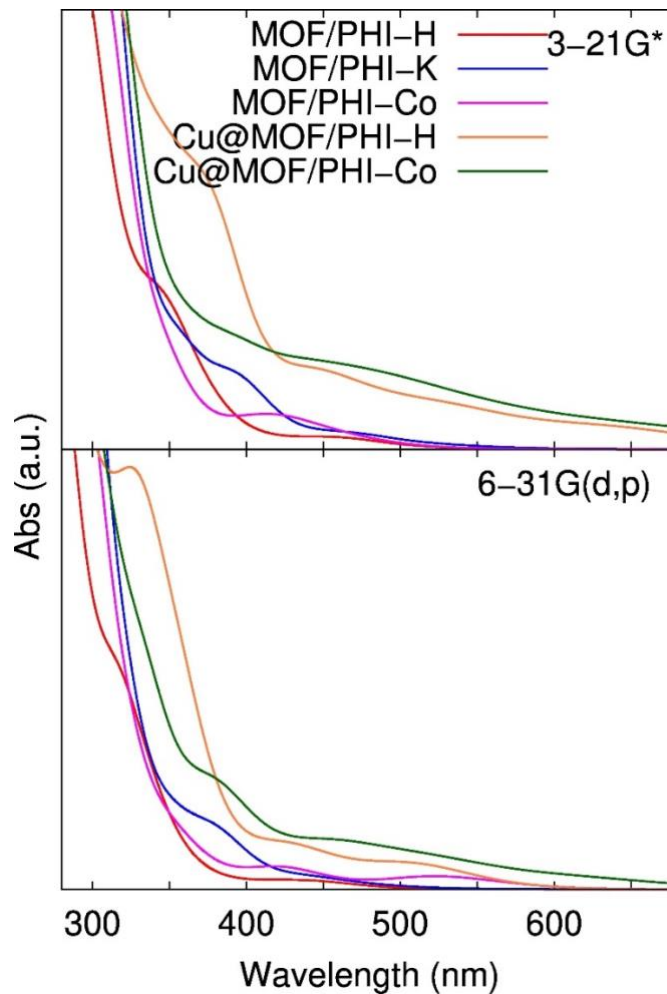
Figure S9. sTDA simulated absorption spectra for all heterojunction cluster models considered in this work, as estimated by employing 3-21G* (top) and 6-31G(d,p) (bottom panel) basis sets.

S1.3. MOF/PHI-M device heterojunction models

To investigate the transport properties of the device heterojunction models, we prepared a series of theoretical molecular junctions with each heterojunction cluster model as the active molecular element in the scattering region. The device heterojunctions were optimized as electronic devices from which we calculated the transport properties. The transmission orbitals were computed to analyse the charge transport between electrodes, as it traverses through the scattering region containing the composite. The current-voltage (*J-V*) characteristics through the device junction are given by the Landauer–Büttiker formula:[30]

$$I_\sigma(V) = \frac{2e}{h} \int_{u_L}^{u_R} T_\sigma(E,V)[f(E - u_L) - f(E - u_R)]dE \qquad \text{(Eq. S2)}$$

where $T(E,V)$ is the transmission at a given bias voltage (V), $f(E,E_F)$ is the Fermi–Dirac distribution function and u_L/u_R is the chemical potential of the left (L) and right (R) electrodes. Finally, for spin polarized systems, the spin index ($\sigma = \alpha, \beta$) is considered. The transmission coefficients are obtained from:

$$T_\sigma(E,V) = T_r[\tau_R(E,V)G_C(E,V)\tau_L(E,V)G_C^+(E,V)] \qquad \text{(Eq. S3)}$$

where $G_C(E,V)$ and $G_C^+(E,V)$ are the retarded and advanced Green's functions, and $\tau_{R/L}$ represent the self-energy matrices, which describe the coupling between the electrodes and the central scattering region.
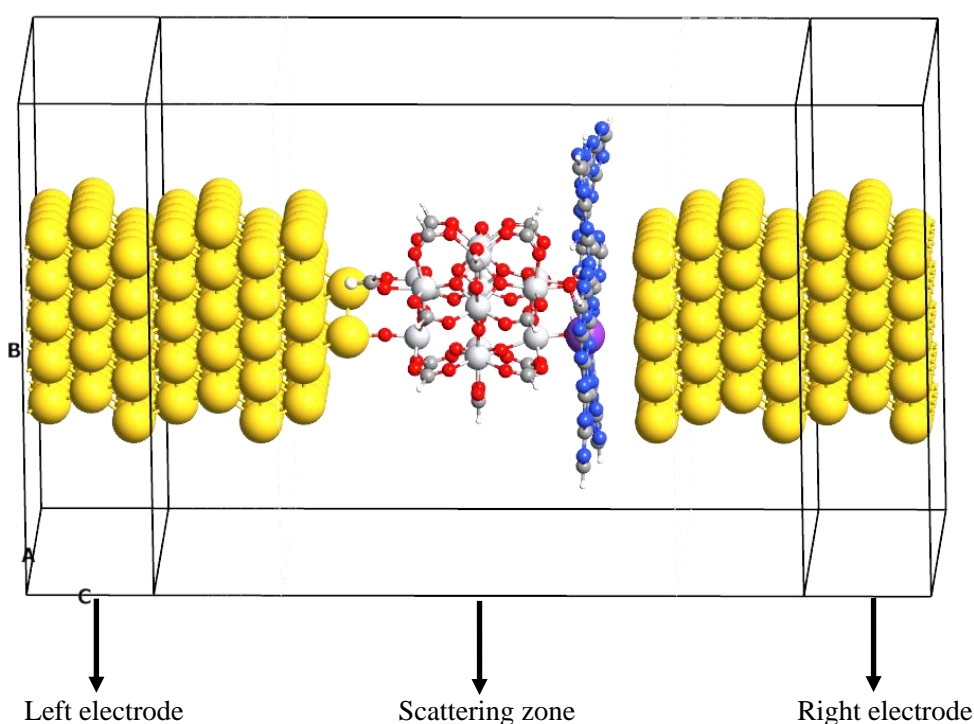
Figure S10. Scheme of the device heterojunction architecture employed in this work. The central scattering zone consists in four Au layers on the left side, the heterojunction cluster models, and for Au gold layers on the right side. The MOF fragment is anchoring by terminal O group to an Au atom in a hollow position on the left side of the surface. We used (5x5) unit cell and 25 gold atoms per layer. The asymmetric configuration ([ABC]ABCA–Mol–CABC[ABC]) was set to provide a enough number of screening layers.[31]

We then evaluated the influence of the number of these covalent bonds by investigating the device junction characteristics of the MOF/PHI-K$^+$ composite attached to the Au surface via

one, two and three contacts. Interestingly, the occupied levels lie closer to the Au Fermi level when increasing the coupling with the electrode (i.e. the number of contacts). However, both transmission and projected device density of state (PDDOS) features appear well converged (with respect to the number of contacts) with already two contacts (see Figure S15). As one may expect the amount of current crossing along the device heterojunction increases with the number of contacts, especially when a significant negative voltage difference is applied between the electrodes. Nonetheless, both two- and three-contacted device heterojunctions exhibited analogous asymmetric J-V curves, thus yielding to identical rectification ratio (RR) values (see Figure S16).
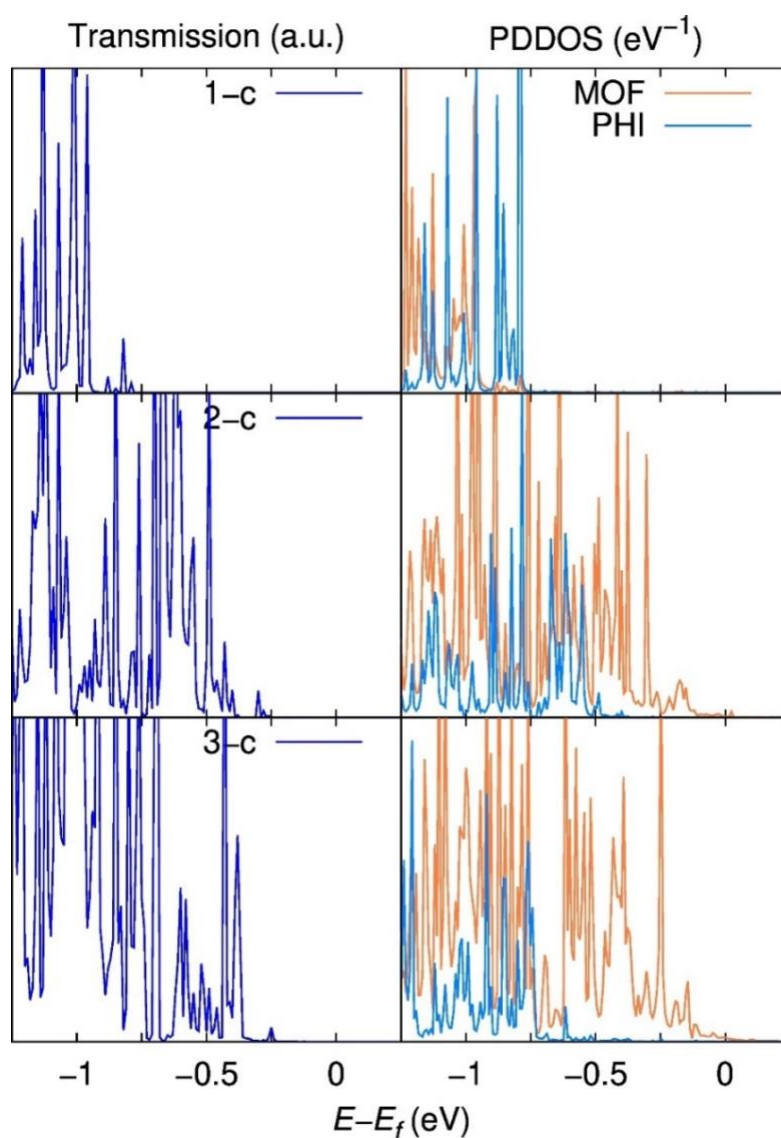
Figure S11. Equilibrium transmission spectra (left) and PDDOS along the MOF (orange) and PHI (bright blue) components (right panels), MOF/PHI-K$^+$ device heterojunction models attached to the bottom Au electrode via one (1-c), two (2-c) and three (3-c) contacts.
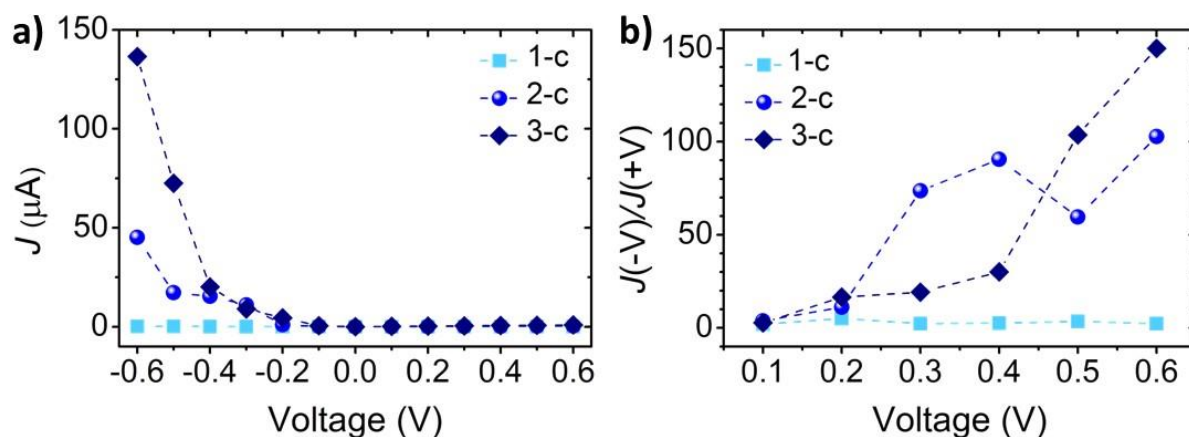
Figure S12. a) Current-voltage (J-V) curves and b) rectification ratios RR(V)=J(-V)/J(V) for the a) MOF/PHI-K$^+$ device heterojunctions attached to the bottom Au electrode via one (1-c), two (2-c) and three (3-c) contacts.

S2. Supporting data of the manuscript

S2.1. Geometric properties

Table S13. Computed relative averaged interaction energies along the FF-MD trajectories of the MOF/PHI-M heterojunctions, as calculated by extracting the difference between the total energy of the system ($E_{MOF/PHI-M}$) and its isolated MOF (E_{MOF})and PHI-M (E_{PHI-M}) components. Note that the interaction energy of the most stable heterojunction (MOF/PHI-K$^+$) was set as reference energy value.

System	Interaction Energy (eV)
MOF/PHI-H	1.97
MOF/PHI-K$^+$	0
MOF/PHI-Co^{2+}	1.14
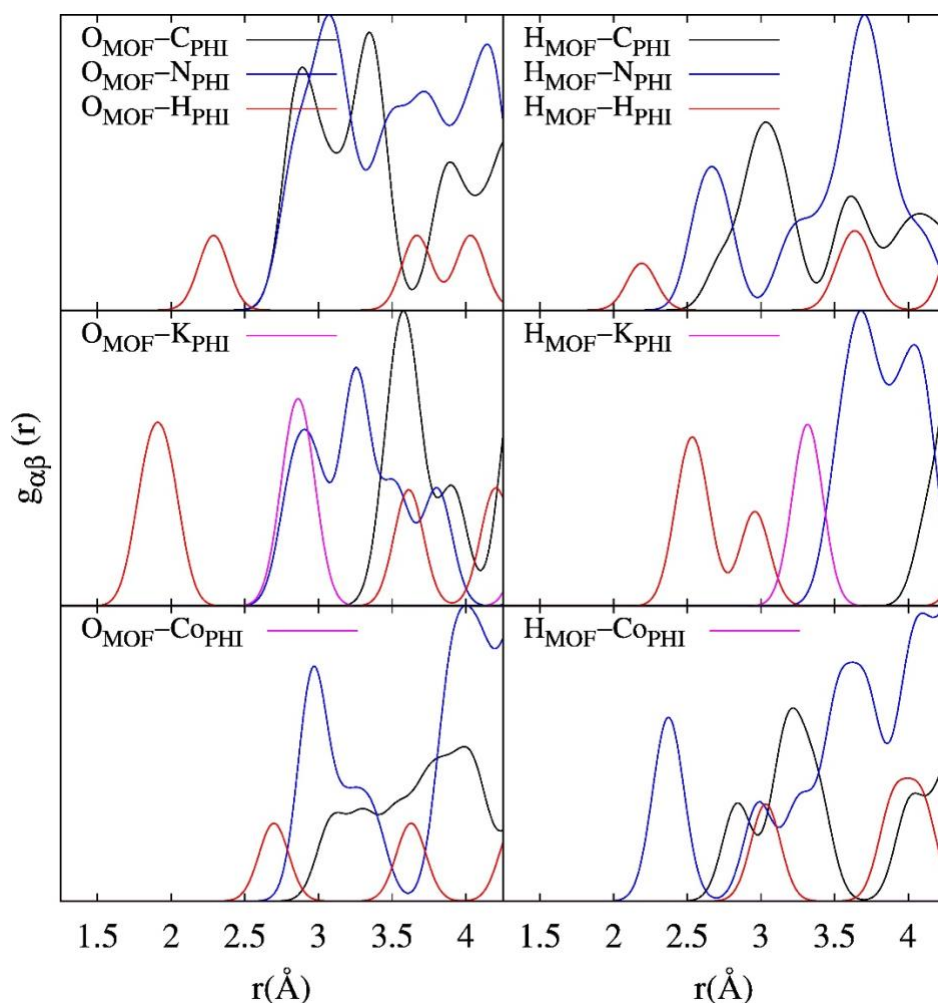
Figure S13. Radial distribution functions between the O (left) and H (right panels) atoms conforming the MOF's OH-terminations, and the C (black), N (blue), H (red) and M=K$^+$, Co^{2+} (magenta) atoms of the PHI-M layer within the MOF/PHI-H (top), MOF/PHI-K$^+$ (middle), and MOF/PHI-Co^{2+} (bottom) heterojunction cluster models. These distributions have been built via convolution of gaussian functions of σ=0.1 eV centred at the discrete interatomic distances obtained from the static relaxed geometries, and they were employed to mimic thermal motion.

S2.2. Electronic properties

Table S14. Computed relative interaction energies in eV for the MOF/PHI-M heterojunction cluster models studied in this work, estimated as the difference between the energies of the composite ($E_{MOF-PHI}$) and the MOF (E_{MOF}) and PHI (E_{PHI}) components. Note that the energy of the most stable heterojunction cluster model (MOF/PHI-K$^+$) was set as reference energy value.

System	Interaction Energy (eV)
MOF/PHI-H	1.91
MOF/PHI-K$^+$	0
MOF/PHI-Co^{2+}	1.72
Cu$^+$@MOF/PHI-Co^{2+}	1.58

MOF/PHI-H   **MOF/PHI-K$^+$**   **MOF/PHI-Co^{2+}**   **Cu@MOF/PHI-Co^{2+}**
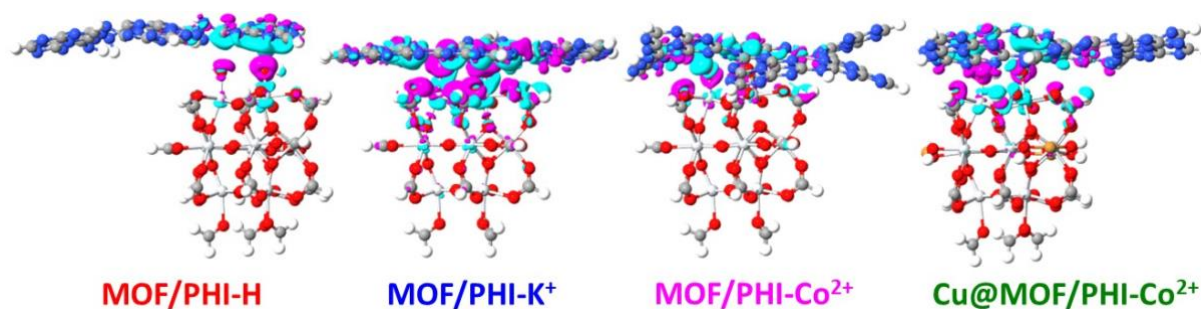
Figure S14. Charge density difference $\Delta\rho$(x,y,z) plots for the MOF/PHI-M heterojunction cluster models studied in this work, calculated as the difference between the charge densities of the composite ($\rho_{MOF-PHI}$) and the MOF (ρ_{MOF}) and PHI (ρ_{PHI}) components. The isovalue used to plot the isodensity was set to 0.001 a.u.

Table S15. Sum of Electrostatic Potential (ESP) charges among the atoms conforming the MOF ($\sum Q_{MOF}$) and PHI ($\sum Q_{PHI}$) fragments of the MOF/PHI-M heterojunction cluster models.

Interface	$\sum Q_{MOF}$	$\sum Q_{PHI}$
MOF/PHI-H	-0.056	0.056
MOF/PHI-K$^+$	0.009	-0.009
MOF/PHI-Co^{2+}	-0.009	0.009
Cu$^+$@MOF/PHI-Co^{2+}	0.059	-0.059
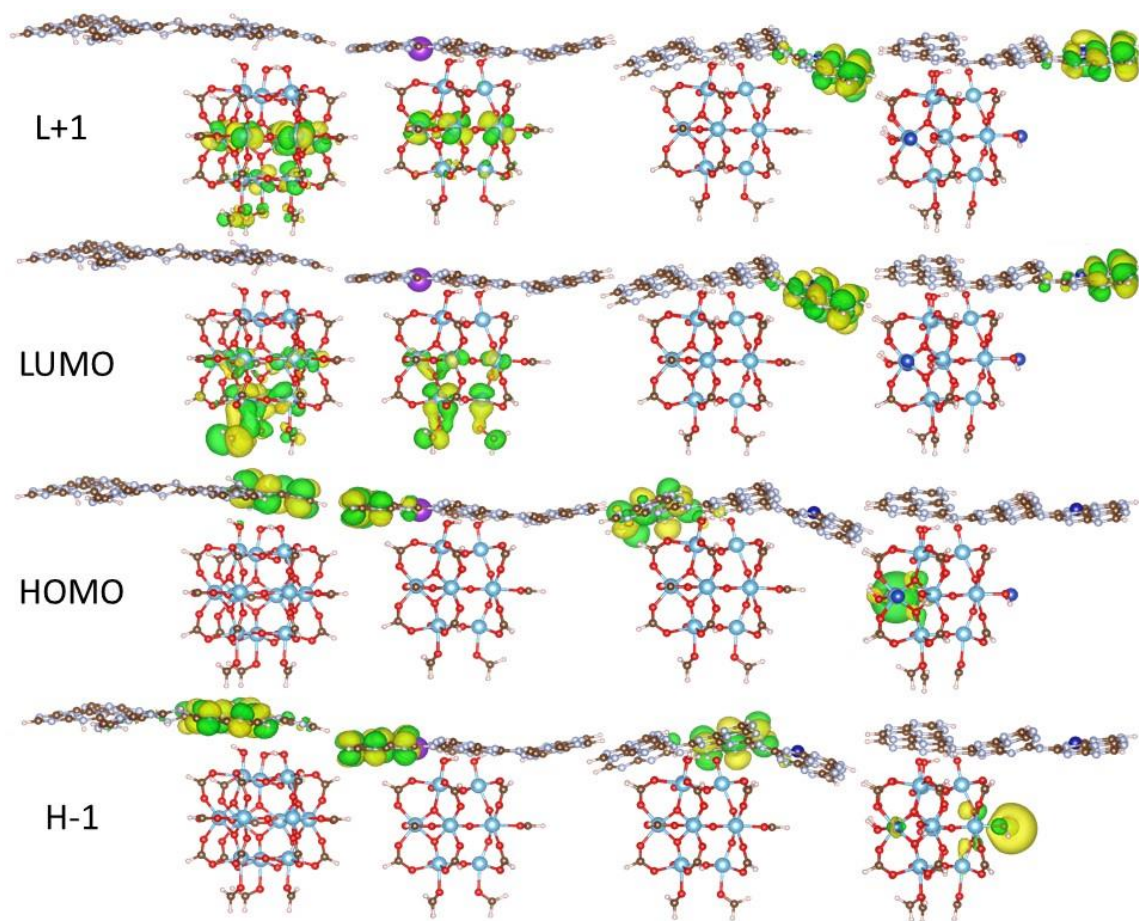
Figure S15. Frontier molecular orbital (FMO) shapes for the MOF/PHI-H, MOF/PHI-K$^+$, MOF/PHI-Co^{2+} and Cu$^+$@MOF/PHI-Co^{2+} heterojunction cluster models (from the right to the left). The isovalue used for the isodensity plots was set to 0.02 a.u.
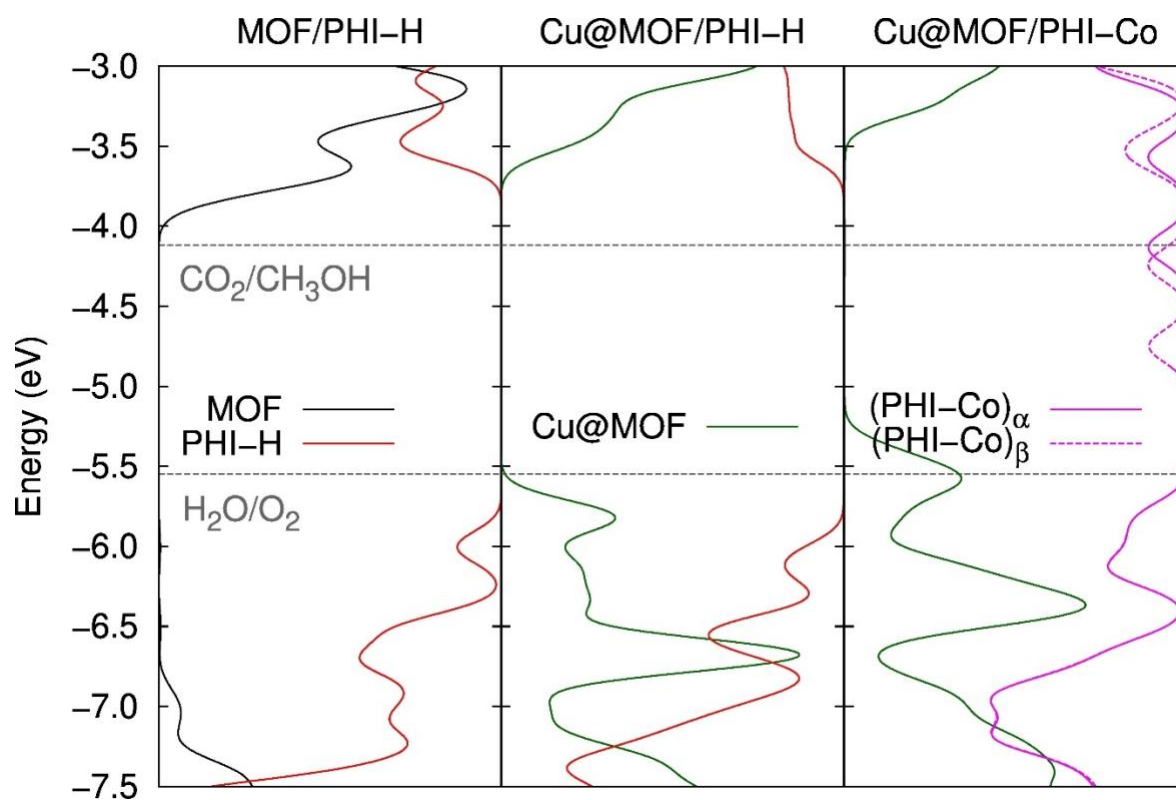
Figure S20. Projected density of states (PDOS) along the MOF (right) and PHI (left part of the graphs) fragments for MOF/PHI-H, $Cu^+@MOF/PHI$-H and $Cu^+@MOF/PHI$-Co^{2+} heterojunction cluster models (from the left to the right); as obtained from Mulliken population analysis. Horizontal dashed lines represent the energies for the CO_2/CH_3OH and O_2/H_2O reaction potentials with respect to the vacuum level.

S2.3. Optical properties

Table S16. Excited state properties for the main vertical transitions conforming the simulated spectra depicted in Figures 5-a and S21: number of state (n), exciton energies (E) and wavelengths (λ), oscillator strengths (f) and main occupied-virtual orbital transitions composing the state, with their corresponding weight ($C_{o \to v}$).

| System	n	E_x (eV)	λ (nm)	f	Transition	$C_{o \to v}$
MOF/ PHI-H	13	2.63	471	0.020	H→L+11	0.99
	115	3.25	381	0.026	H-7→L+7	0.64
	182	3.45	359	0.029	H→L+29	0.56
	239	3.58	347	0.113	H-19→L+1	0.46
	424	3.87	321	0.054	H-22→L+7	0.48
	565	4.04	307	0.061	H-35→L+2	0.31
MOF/ PHI-K$^+$	60	2.34	530	0.010	H→L+18	1.00
	125	2.65	468	0.024	H→L+25	0.88
	293	3.13	396	0.098	H→L+33	0.62
	481	3.52	353	0.089	H-3→L+33	0.59
	777	3.94	315	0.328	H-25→L+9	0.60
	879	4.06	306	0.158	H-23→L+12	0.40
MOF/ PHI-Co^{2+}	39	2.66	467	0.010	(H-12→L)$_\beta$	0.82
	100	2.96	419	0.020	(H-16→L)$_\alpha$	0.52
	602	3.77	329	0.030	(H-8→L+10)$_\alpha$	0.40
	960	4.02	308	0.051	(H-22→L+7)$_\alpha$	0.26
Cu$^+$@MOF/ PHI-H	25	1.92	646	0.016	H-1→L+5	0.78
	41	2.00	619	0.022	H-4→L+3	0.76
	286	2.72	456	0.018	H-6→L+19	0.53
	360	2.89	429	0.021	H-11→L+18	0.43
	565	3.29	377	0.224	H-21→L+4	0.74
Cu$^+$@MOF/ PHI-Co^{2+}	78	1.74	714	0.010	(H→L+6)$_\beta$	0.66
	124	1.90	653	0.017	(H-2→L+7)$_\beta$	0.54
	481	2.42	511	0.011	(H-10→L+10)$_\alpha$	0.33
	581	2.54	489	0.011	(H-29→L)$_\beta$	0.68
	627	2.59	479	0.012	(H-31→L)$_\beta$	0.84
	814	2.79	444	0.012	(H-3→L+27)$_\alpha$	0.53
	862	2.84	436	0.032	(H-3→L+29)$_\beta$	0.42
	1186	3.18	391	0.032	(H-3→L+40)$_\beta$	0.45
	1511	3.41	363	0.023	(H-21→L+4)$_\alpha$	0.61
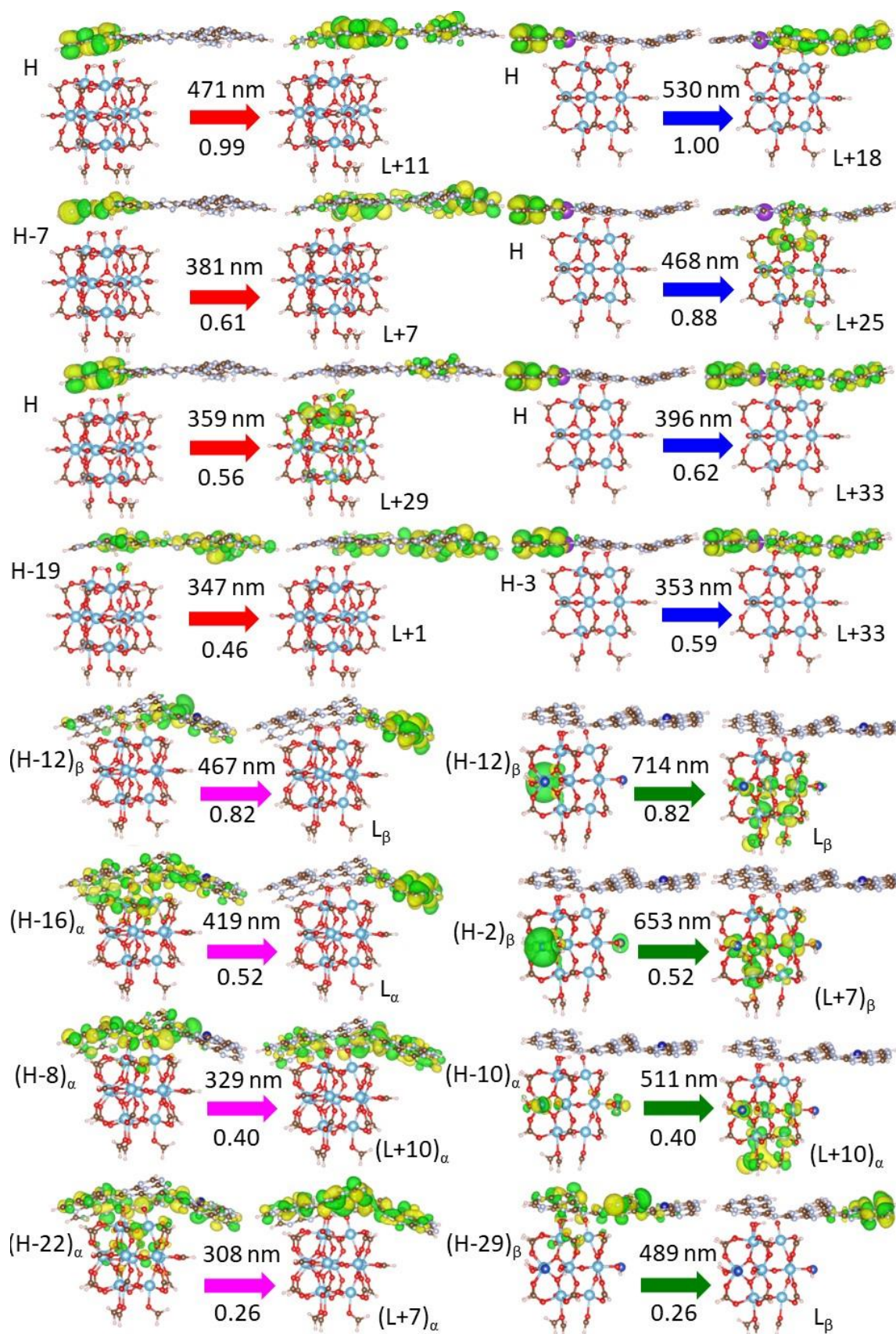
Figure S16. MOs isodensity plots for the main occupied-virtual orbital transitions composing the spectra depicted in Figure 5-a. The isovalue used to plot the isodensity was set to 0.02 a.u.
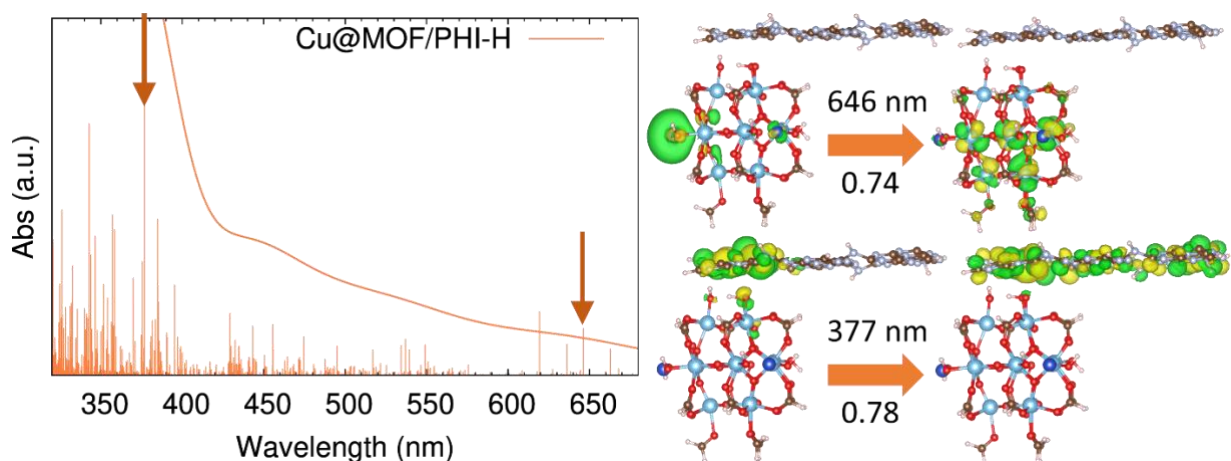
Figure S17. Simulated spectrum for Cu$^+$@MOF/PHI-H heterojunction cluster model (left) and MOs isodensity plots for the occupied-virtual orbital transitions highlighted by vertical arrows in the spectrum (right). The isovalue used to plot the isodensity was set to 0.02 a.u.

S2.4. Device junction characteristics

Table S17. Contact distances in Å between the Au electrodes and the MOF (orange) and PHI (blue) moieties: Au-O_{MOF} bond distances and closest distances between the top electrode and the atoms conforming the PHI layer.

Device heterojunction	(Au-O_{MOF})$_1$	(Au-O_{MOF})$_2$	Au-C_{PHI}	Au-N_{PHI}	Au-H_{PHI}	Au-M_{PHI}
MOF/PHI-H	2.19	1.88	3.54	3.17	2.95	-
MOF/PHI-K$^+$	2.25	2.11	3.66	3.74	4.07	4.07
MOF/PHI-Co^{2+}	2.25	2.23	3.67	3.42	3.71	5.13
Cu$^+$@MOF/PHI-Co^{2+}	2.18	2.20	3.35	3.20	3.26	5.50
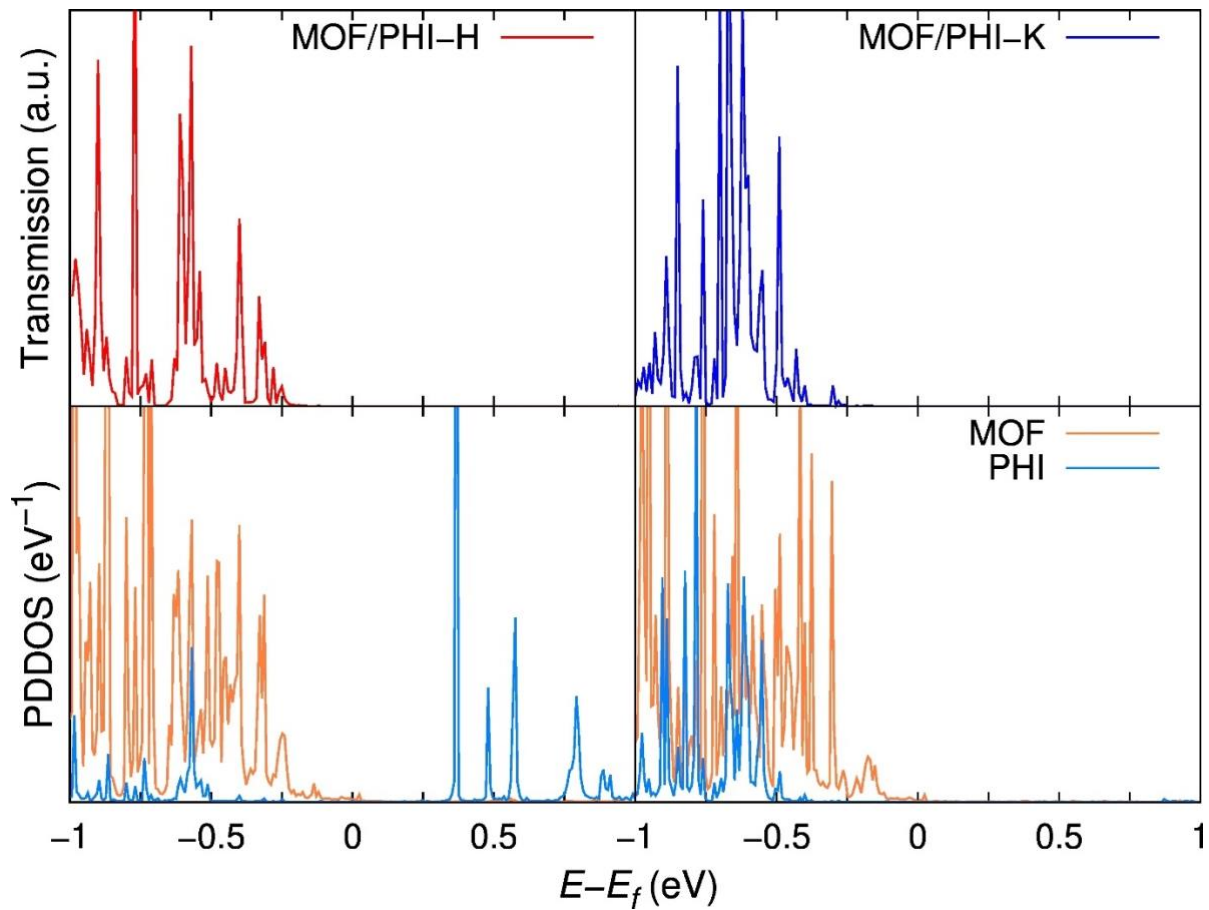
Figure S18. Equilibrium transmission spectra (top) and projected device density of states (PDDOS) along the MOF (orange) and PHI (bright blue) components (bottom panels), for the MOF/PHI-H (left) and MOF/PHI-K$^+$ (right) device heterojunctions.
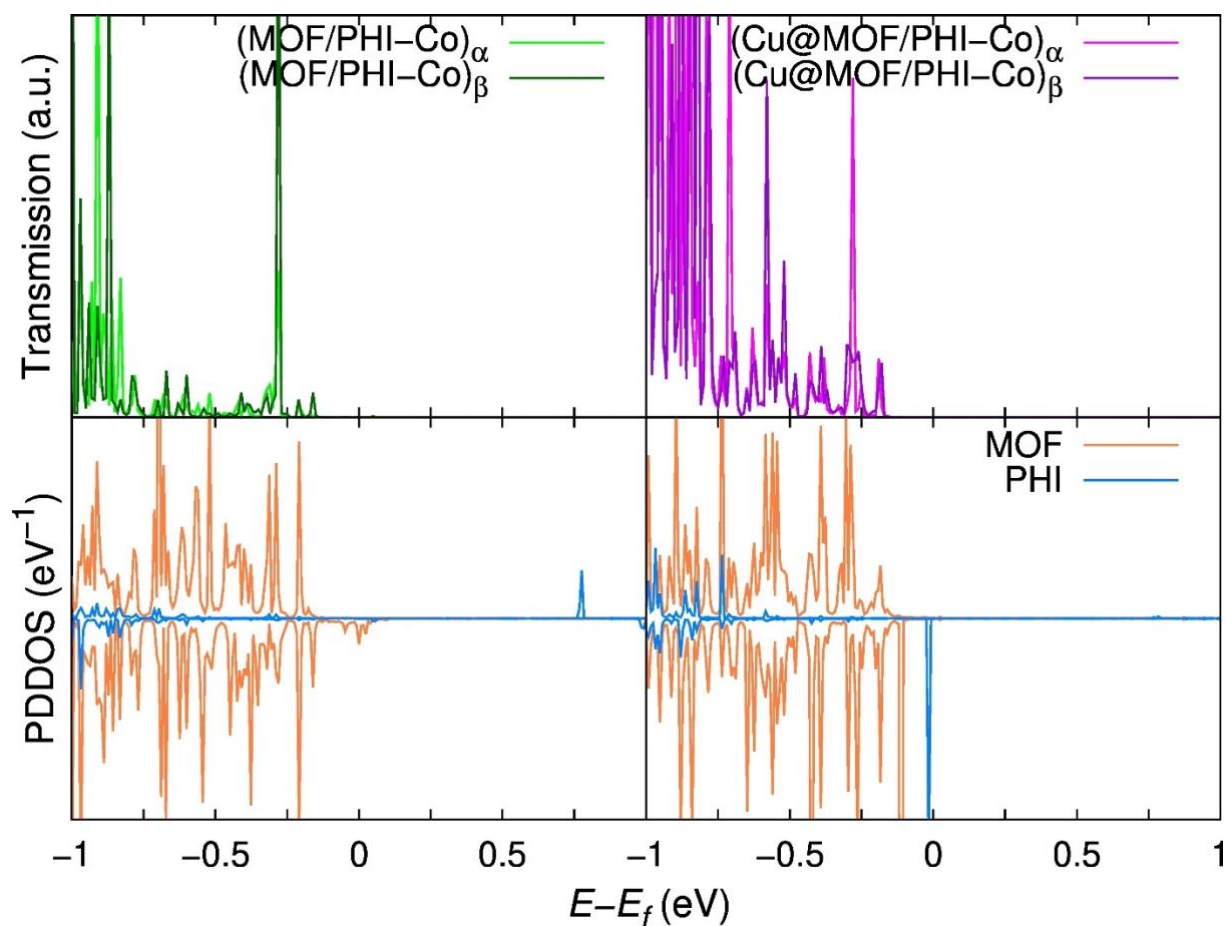
Figure S19. Equilibrium transmission spectra (top) and PDDOS along the MOF (orange) and PHI (bright blue) components (down panels), for the MOF/PHI-Co^{2+} (left) and MOF/PHI-K$^+$ (right) device heterojunctions. Bright and dark colours are used to depict the spin up and down contributions, respectively, for the transmission spectra of the MOF/PHI-Co^{2+} (green) and MOF/PHI-K$^+$ (violet) device heterojunctions.
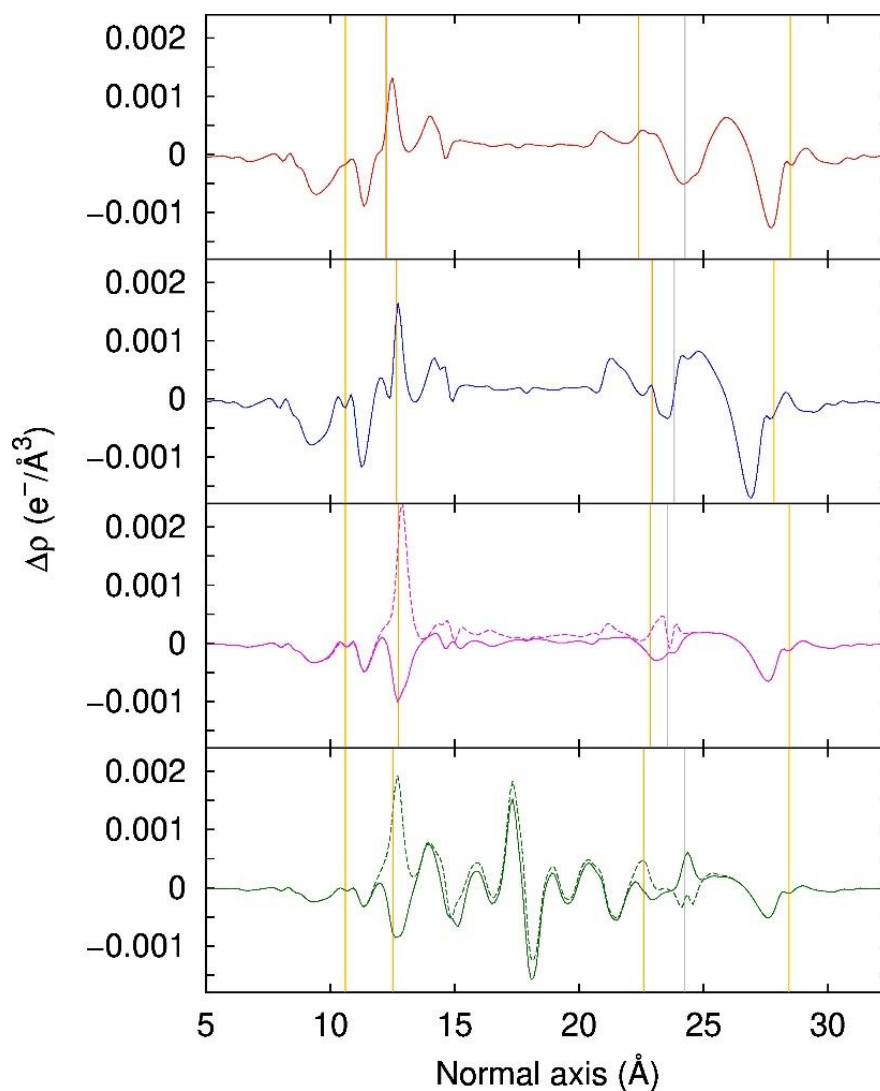
Figure S20. Averaged charge density difference along the normal direction $\Delta\rho(z)$ for the $Au_L|MOF/PHI-M|Au_R$ device heterojunctions studied in this work, calculated as the difference between the charge densities of the MOF-PHI heterojunction cluster ($\rho_{MOF-PHI}$) and the MOF (ρ_{MOF}), PHI (ρ_{PHI}) and electrode slab (Au_L/Au_R) fragments. Yellow, orange and grey vertical lines represent the averaged position of the interfacial Au layers, the MOF surface atoms and the PHI layer, respectively.
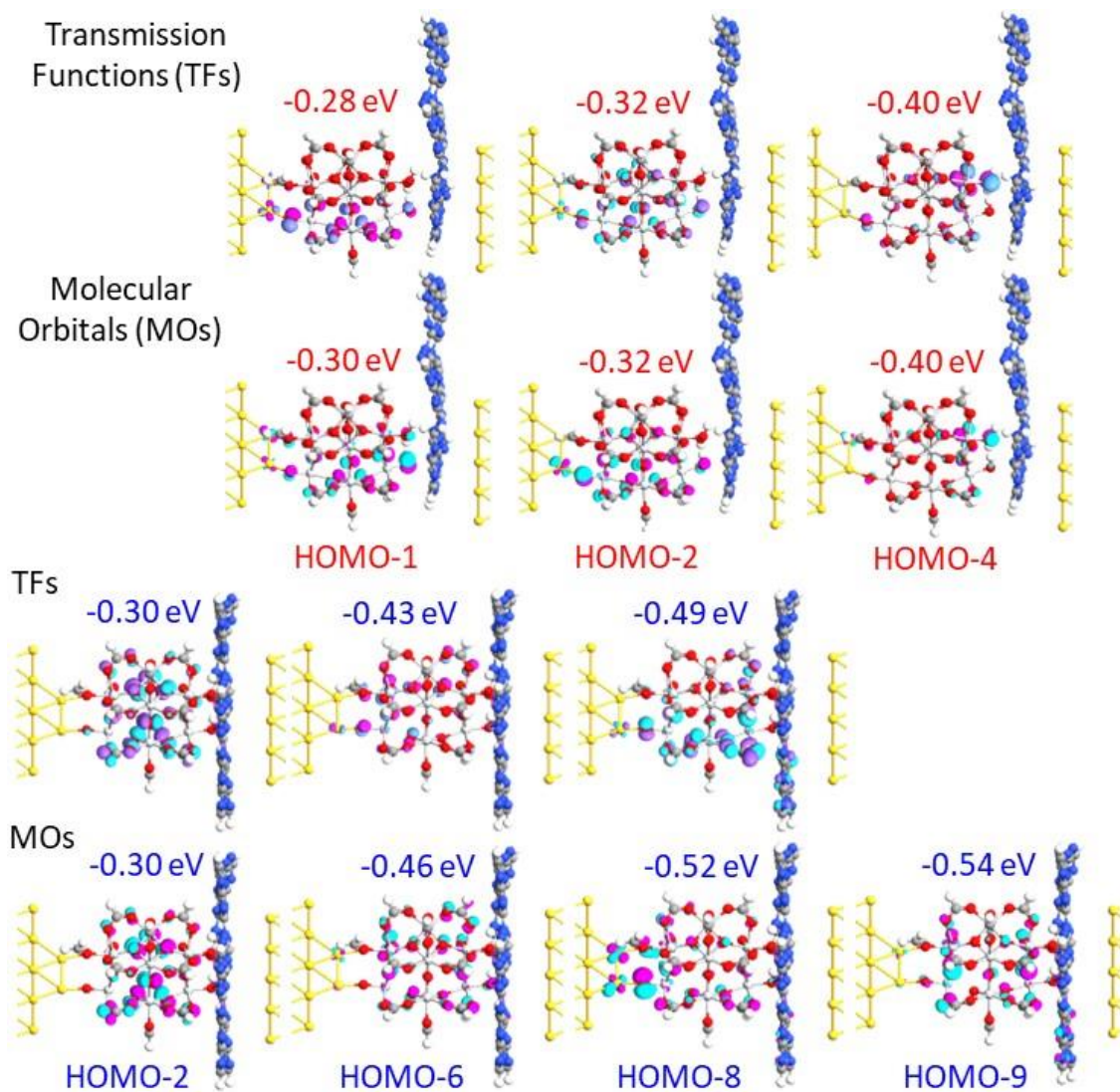
Figure S21. Transmission functions (TFs) (top part) and corresponding molecular orbitals (MOs) below for the closest signals to the Fermi level from the transmission spectra across the MOF/PHI-H (red) and MOF/PHI-K$^+$ (blue) device heterojunctions.
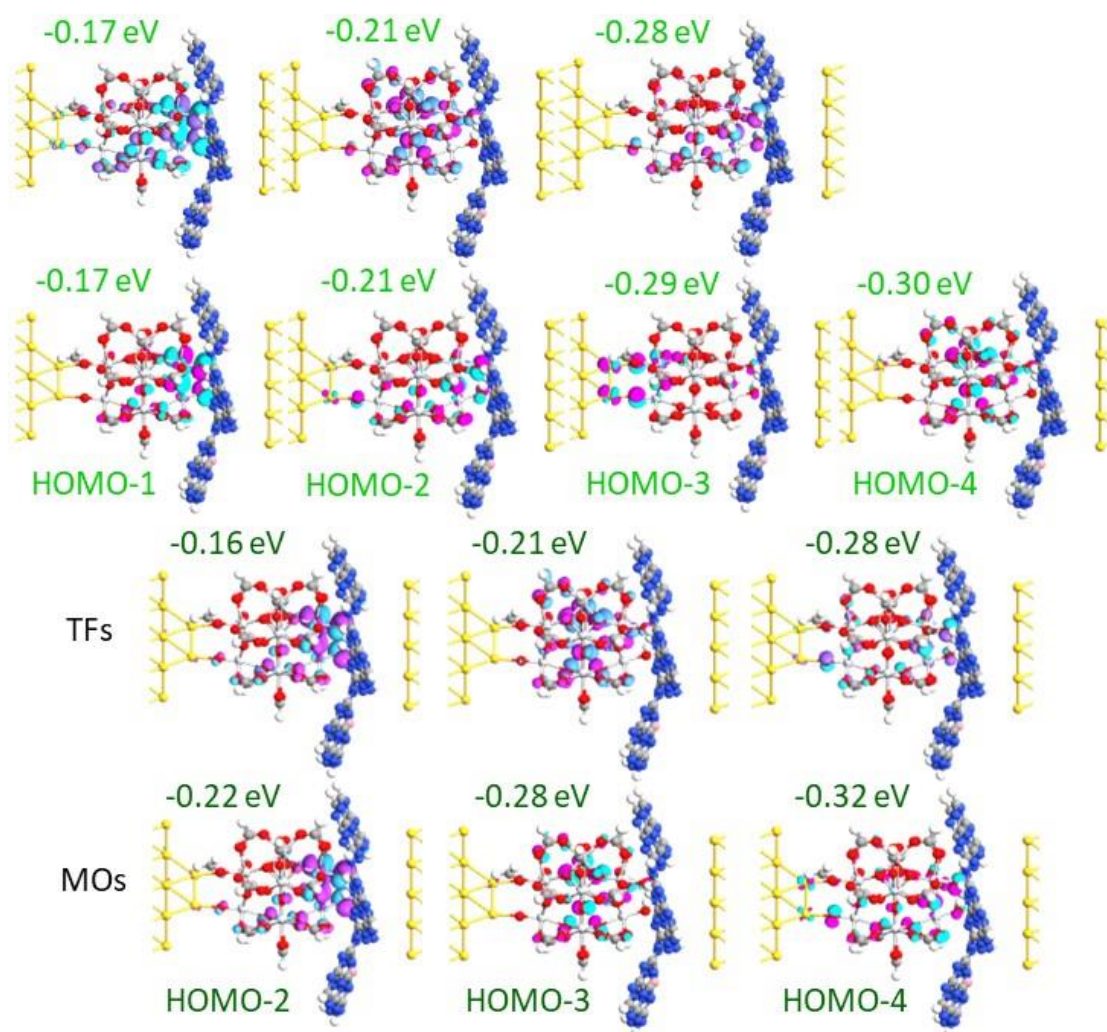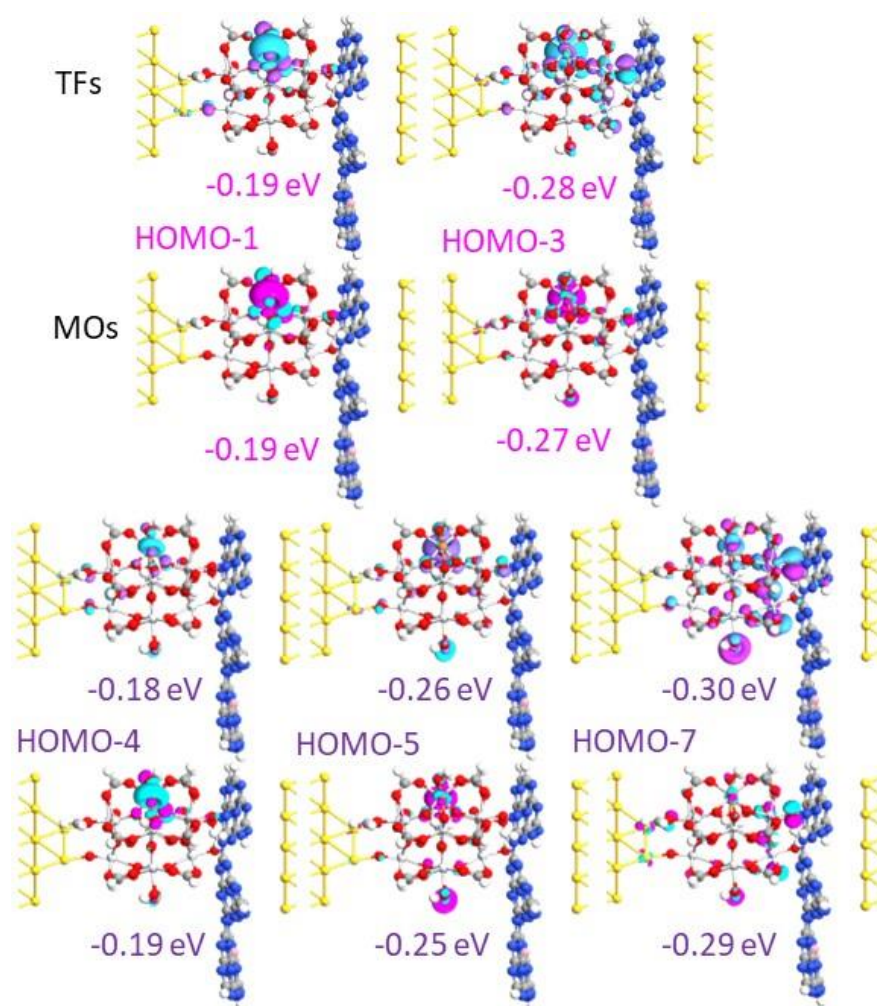
Figure S22. TFs (top part) and corresponding MOs below for the closest signals to the Fermi level from the transmission spectra across the MOF/PHI-Co^{2+} device heterojunctions in their spin up (bright green) and down (dark green) configurations.

Figure S23. TFs (top part) and corresponding MOs below for the closest signals to the Fermi level from the transmission spectra across the Cu^+@MOF/PHI-Co^{2+} based device heterojunctions in their spin up (magenta) and down (purple) configurations.

Table S18. Computed values of the conductance (G_0) across the Au_L|MOF/PHI|Au_R device heterojunctions investigated in this work.

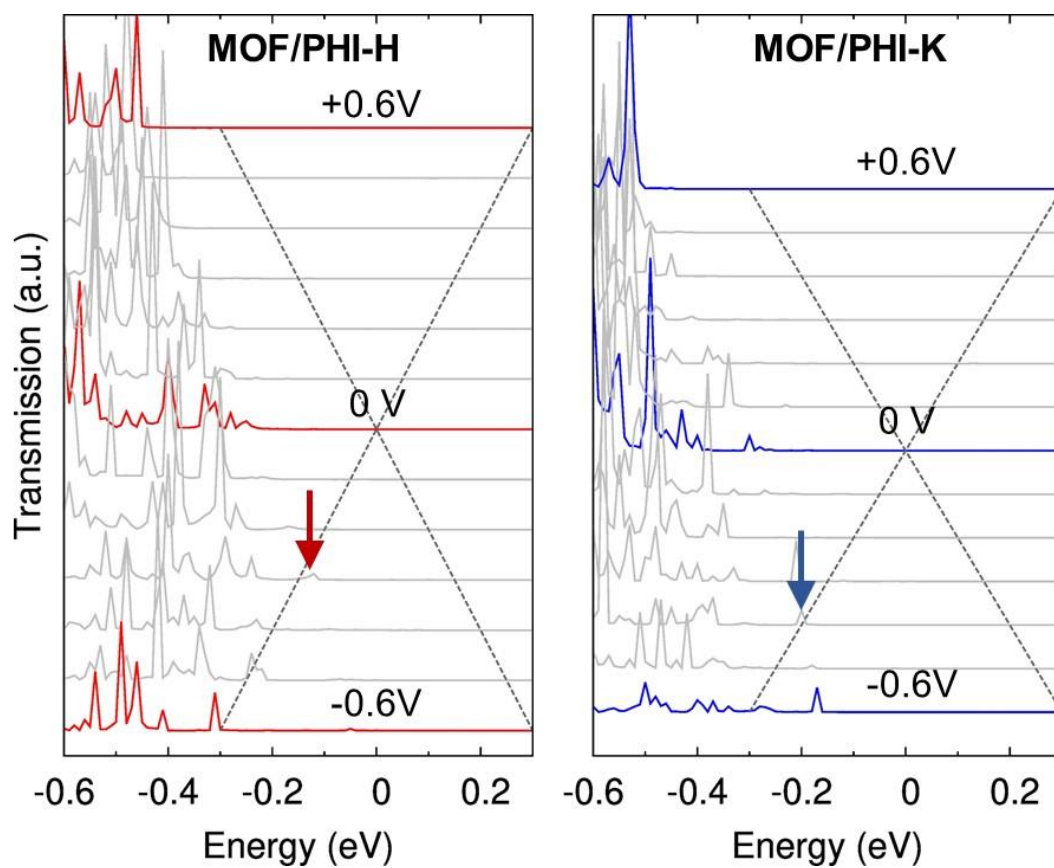| Device heterojunction	G_0 (µA)	
spin	α	β
MOF/PHI-H	75.0	
MOF/PHI-K^+	11.0	
MOF/PHI-Co^{2+}	34.6	2330
Cu^+@MOF/PHI-Co^{2+}	24.6	95.9

Figure S24. Transmission spectra as a function of the applied voltage for the MOF/PHI-H (left) and MOF/PHI-K$^+$ (right panel) device heterojunctions. Grey dashed lines are used to delimit the voltage windows, whereas vertical arrows are employed to highlight the applied bias where the closest transmission peak to the Fermi level gets inside the voltage window.
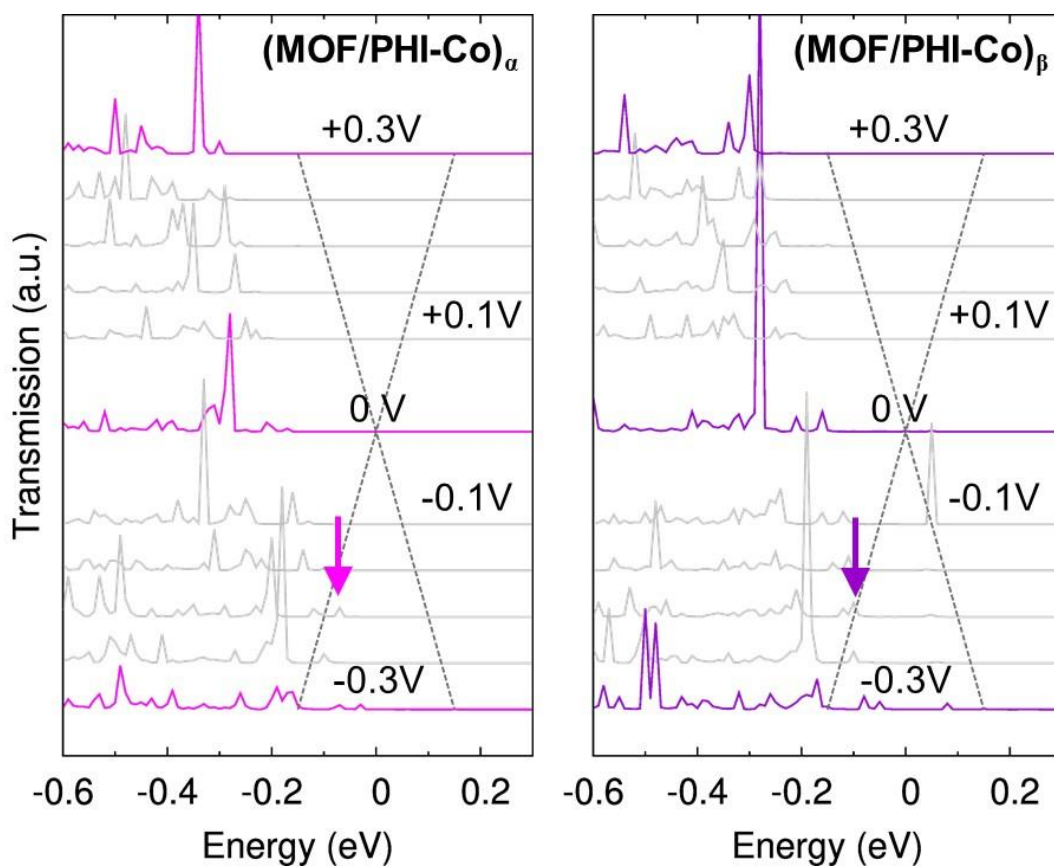
Figure S30. Transmission spectra as a function of the applied voltage for the MOF/PHI-Co^{2+} device heterojunction in their spin up (left) and down (right) configurations. Grey dashed lines are used to delimit the voltage window, whereas vertical arrows are employed to highlight the applied bias where the closest transmission peak to the Fermi level gets inside the voltage window.
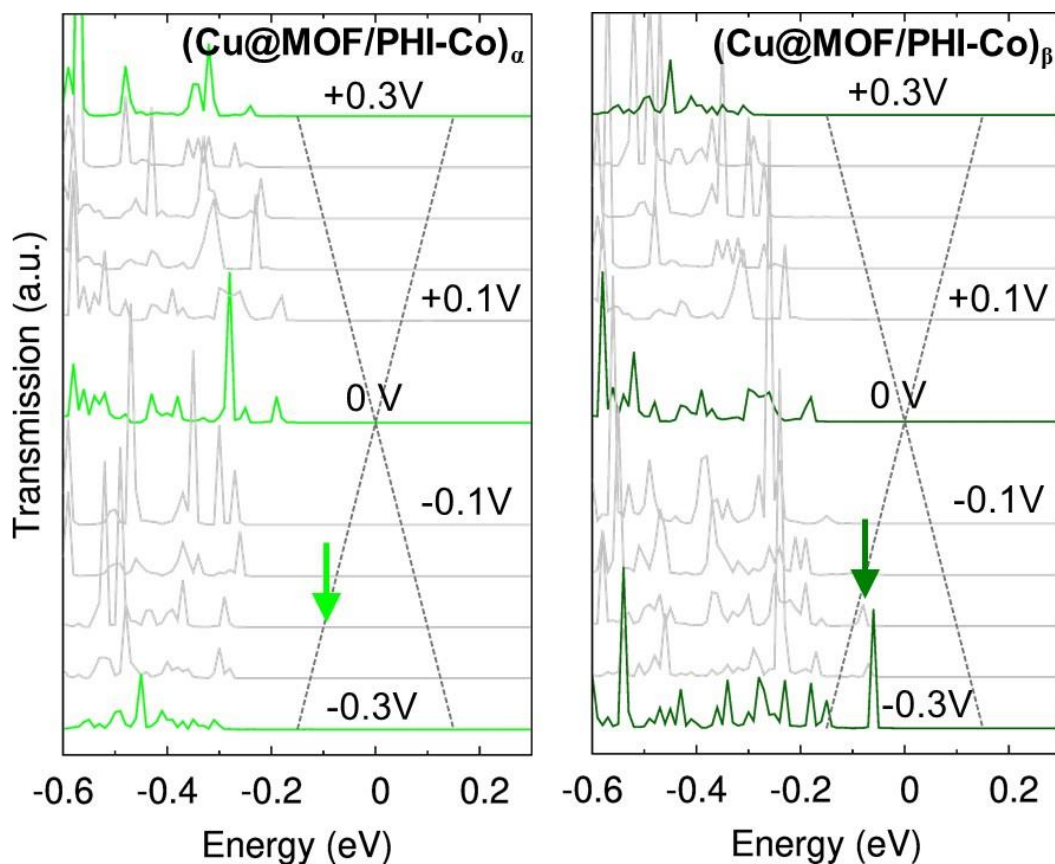
Figure S25. Transmission spectra as a function of the applied voltage for the Cu^+@MOF/PHI-Co^{2+} device heterojunction in their spin up (left) and down (right) configurations. Grey dashed lines are used to delimit the voltage window, whereas vertical arrows are employed to highlight the applied bias where the closest transmission peak to the Fermi level gets inside the voltage window.
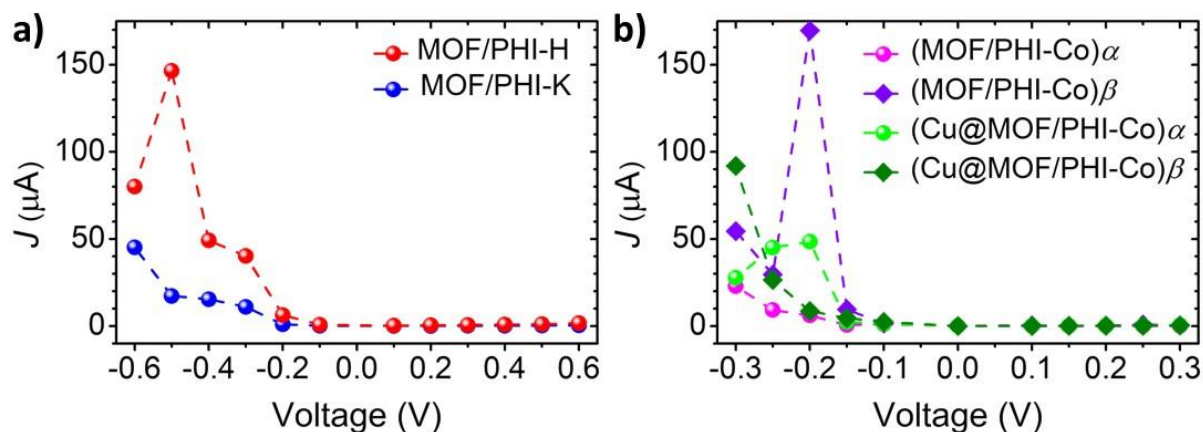

Figure S26. Current-voltage (J-V) curves for the a) MOF/PHI-H (red) vs MOF/PHI-K^+ (blue) and b) MOF/PHI-Co^{2+} (magenta/purple for spin up/down) vs Cu^+@MOF/PHI-Co^{2+} (bright/dark green for spin up/down) device heterojunctions.

Figure S27. Rectification ratios RR(V)=J(-V)/J(V) for the a) MOF/PHI-H (red) vs MOF/PHI-K$^+$ (blue) and b) MOF/PHI-Co^{2+} (magenta/purple for spin up/down) vs Cu$^+$@MOF/PHI-Co^{2+} (bright/dark green for spin up/down) device heterojunctions.

S3. References
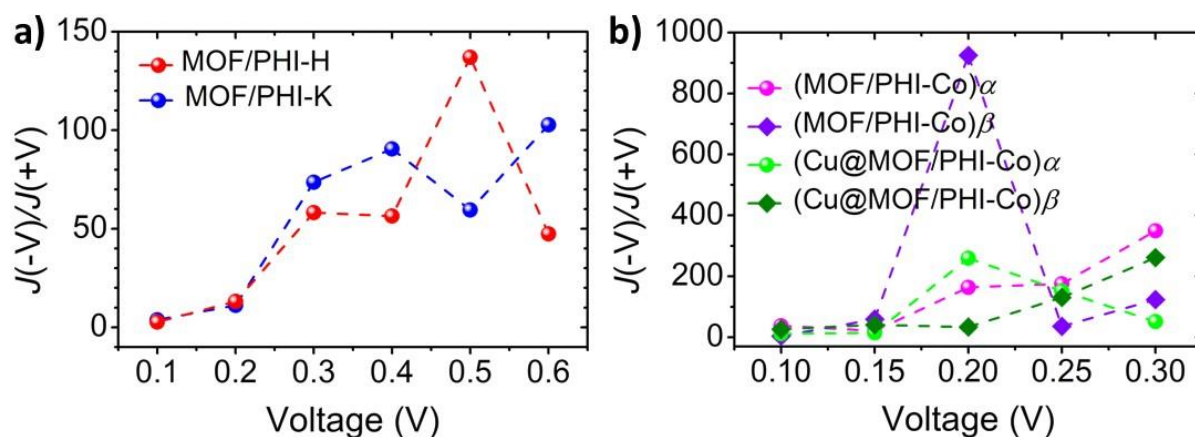
1   G. Kresse and J. Hafner, *Phys. Rev. B*, 1993, **47**, 558–561.

2   M. Dupuy, *ESAIM Math. Model. Numer. Anal.*, 2020, **54**, 25–58.

3   J. P. Perdew, K. Burke and M. Ernzerhof, *Phys. Rev. Lett.*, 1996, **77**, 3865–3868.

4   J. Moellmann and S. Grimme, *J. Phys. Chem. C*, 2014, **118**, 7615–7621.

5   S. Wang, T. Kitao, N. Guillou, M. Wahiduzzaman, C. Martineau-Corcos, F. Nouar, A. Tissot, L. Binet, N. Ramsahye, S. Devautour-Vinot, S. Kitagawa, S. Seki, Y. Tsutsui, V. Briois, N. Steunou, G. Maurin, T. Uemura and C. Serre, *Nat. Commun.*, 2018, **9**, 1–9.

6   A. K. Rappé, C. J. Casewit, K. S. Colwell, W. A. Goddard and W. M. Skiff, *J. Am. Chem. Soc.*, 1992, **114**, 10024–10035.

7   S. Pronk, S. Páll, R. Schulz, P. Larsson, P. Bjelkmar, R. Apostolov, M. R. Shirts, J. C. Smith, P. M. Kasson, D. Van Der Spoel, B. Hess and E. Lindahl, *Bioinformatics*, 2013, **29**, 845–854.

8   W. L. Jorgensen, D. S. Maxwell and J. Tirado-Rives, *J. Am. Chem. Soc.*, 1996, **118**, 11225–11236.

9   J. P. Perdew, K. Burke and M. Ernzerhof, *Phys. Rev. Lett.*, 1996, **77**, 3865–3868.

10   S. Grimme, J. Antony, S. Ehrlich and H. Krieg, *J. Chem. Phys.*, 2010, **132**, 154104.

11   J. E. Hirsch, *Phys. Rev. Lett.*, 2001, **87**, 206402.

12   M. Capdevila-Cortada, Z. Łodziana and N. López, *ACS Catal.*, 2016, **6**, 8370–8379.

13 M. J. van Setten, M. Giantomassi, E. Bousquet, M. J. Verstraete, D. R. Hamann, X. Gonze and G. M. Rignanese, *Comput. Phys. Commun.*, 2018, **226**, 39–54.

14 S. Smidstrup, T. Markussen, P. Vancraeyveld, J. Wellendorff, J. Schneider, T. Gunst, B. Verstichel, D. Stradi, P. A. Khomyakov, U. G. Vej-Hansen, M. E. Lee, S. T. Chill, F. Rasmussen, G. Penazzi, F. Corsetti, A. Ojanperä, K. Jensen, M. L. N. Palsgaard, U. Martinez, A. Blom, M. Brandbyge and K. Stokbro, *J. Phys. Condens. Matter*, 2020, **32**, 015901.

15 J. Heyd, G. E. Scuseria and M. Ernzerhof, *J. Chem. Phys.*, 2003, **118**, 8207–8215.

16 V. A. Rassolov, *J. Comput. Chem.*, 2001, **22**, 976–984.

17 W. R. Wadt and P. J. Hay, *J. Chem. Phys.*, 1985, **82**, 284–298.

18 M. J. Frisch, G. W. Trucks, H. B. Schlegel, G. E. Scuseria, M. A. Robb, J. R. Cheeseman, G. Scalmani, V. Barone, G. A. Petersson, H. Nakatsuji, X. Li, M. Caricato, A. Marenich, J. Bloino, B. G. Janesko, R. Gomperts, B. Mennucci, H. P. Hratchian, J. V. Ortiz, A. F. Izmaylov, J. L. Sonnenberg, D. Williams-Young, F. Ding, F. Lipparini, F. Egidi, J. Goings, B. Peng, A. Petrone, T. Henderson, D. Ranasinghe, V. G. Zakrzewski, J. Gao, N. Rega, G. Zheng, W. Liang, M. Hada, M. Ehara, K. Toyota, R. Fukuda, J. Hasegawa, M. Ishida, T. Nakajima, Y. Honda, O. Kitao, H. Nakai, T. Vreven, K. Throssell, J. J. A. Montgomery, J. E. Peralta, F. Ogliaro, M. Bearpark, J. J. Heyd, E. Brothers, K. N. Kudin, V. N. Staroverov, T. Keith, R. Kobayashi, J. Normand, K. Raghavachari, A. Rendell, J. C. Burant, S. S. Iyengar, J. Tomasi, M. Cossi, J. M. Millam, M. Klene, C. Adamo, R. Cammi, J. W. Ochterski, R. L. Martin, K. Morokuma, O. Farkas, J. B. Foresman and D. J. Fox, 2016, Gaussian Inc., Wallingford CT.

19 G. Kresse and D. Joubert, *Phys. Rev. B - Condens. Matter Mater. Phys.*, 1999, **59**, 1758–1775.

20 M. Iannuzzi, T. Chassaing, T. Wallman and J. Hutter, *Chimia (Aarau).*, 2005, **59**, 499–503.

21 J. Hutter, M. Iannuzzi, F. Schiffmann and J. Vandevondele, *Wiley Interdiscip. Rev. Comput. Mol. Sci.*, 2014, **4**, 15–25.

22 C. M. Rueda-Navarro, M. Cabrero-Antonino, P. Escamilla, V. Díez-Cabanes, D. Fan, P. Atienzar, B. Ferrer, I. Vayá, G. Maurin, H. G. Baldoví and S. Navalón, *Nano Res.*, 2023, **17**, 4134–4150.

23 R. L. Martin, *J. Chem. Phys.*, 2003, **118**, 4775–4777.

24 S. Liu, V. Diez-Cabanes, D. Fan, P. Lyu and G. Maurin, *Prep.*

25 S. Liu, V. Diez-Cabanes, D. Fan, L. Peng, Y. Fang, M. Antonietti and G. Maurin, *ACS Catal.*, 2024, **14**, 2562–2571.

26 S. K. Sahoo, I. F. Teixeira, A. Naik, J. Heske, D. Cruz, M. Antonietti, A. Savateev and T. D. Kühne, *J. Phys. Chem. C*, 2021, **125**, 13749–13758.

27 M. A. R. da Silva, I. F. Silva, Q. Xue, B. T. W. Lo, N. V. Tarakina, B. N. Nunes, P. Adler, S. K. Sahoo, D. W. Bahnemann, N. López-Salas, A. Savateev, C. Ribeiro, T. D. Kühne, M. Antonietti and I. F. Teixeira, *Appl. Catal. B Environ.*, 2022, **304**, 120965.

28 S.M. Dancoff, *Phys. Rev.*, 1950, **78**, 382–385.

29 M. Pastore, S. Fantacci and F. De Angelis, *J. Phys. Chem. C*, 2013, **117**, 3685–3700.

30 M. Büttiker, Y. Imry, R. Landauer and S. Pinhas, *Phys. Rev. B*, 1985, **31**, 6207–6215.

31 S. Rodriguez-Gonzalez, Z. Xie, O. Galangau, P. Selvanathan, L. Norel, C. Van Dyck, K. Costuas, C. D. Frisbie, S. Rigaut and J. Cornil, *J. Phys. Chem. Lett.*, 2018, **9**, 2394–2403.